

GEOPHYSICS

The Fe-Ni phase diagram and the Earth's inner core structure

Liangrui Wei¹, Zepeng Wu¹, Kai-Ming Ho², Renata M. Wentzcovitch^{3,4,5,6}, Yang Sun^{1*}

The Fe-Ni alloy is believed to be the main component of Earth's core. Yet, a comprehensive understanding of phase equilibria near the melting point of this alloy under core conditions is still lacking, leaving the effect of nickel inconclusive. Using ab initio simulations, we computed Gibbs free energy and phase diagram for liquid and solid solutions of the Fe-Ni alloy under conditions close to the inner core. The Fe-Ni phase diagram provides crucial insights for understanding previous experimental observations and crystallization simulations of the Fe-Ni alloy under core conditions. It also presents complex scenarios for inner core structures, suggesting body-centered cubic (bcc)-liquid coexistence at the inner core boundary and the possibility of multilayer structures consisting of bcc-hexagonal close-packed (hcp) composites within the inner core. Our work clarifies nickel's substantial impact on the inner core structure, providing additional constraints for studying the core's composition and formation.

Copyright © 2025 The Authors, some rights reserved; exclusive licensee American Association for the Advancement of Science. No claim to original U.S. Government Works. Distributed under a Creative Commons Attribution NonCommercial License 4.0 (CC BY-NC).

INTRODUCTION

The Earth's core consists of a liquid outer core (OC) and a solid inner core (IC), primarily made up of iron-nickel alloys and light elements (1, 2). Understanding the crystalline phases in the solid IC is essential for determining the partitioning of light elements and the core's seismic properties. Traditionally, based on the phase diagram of pure iron, the IC is thought to predominantly have a hexagonal close-packed (hcp) structure (3–5). However, because the free energy of the body-centered cubic (bcc) phase can be comparable to that of the hcp phase under core conditions, the possibility of a bcc IC has also been proposed (6, 7).

Elements alloyed with iron can influence the stability of crystalline phases in the IC. While the exact concentration of light elements in the core remains debated (8–13), nickel is present in the OC and IC, with estimated concentrations ranging from 5% to 15% based on cosmochemical and geochemical models (1, 14). Low-pressure, low-temperature experiments have shown that nickel can enhance the stability of the face-centered cubic (fcc) phase over the hcp phase in iron (15–17). However, at high temperatures similar to core conditions, nickel was theoretically found to stabilize the hcp phase over the fcc phase in iron (18). Given that fcc iron is metastable relative to hcp iron, the fcc phase of the Fe-Ni alloy has not been seriously considered for the IC structure (18). The competition between fcc, hcp, and bcc phases in the Fe-Ni alloy under IC conditions remains largely unresolved.

The bcc Fe-Ni alloy was first observed experimentally at pressures above 225 GPa and temperatures exceeding 3400 K (19). However, subsequent experiments did not confirm the existence of the bcc phase in $\text{Fe}_{90}\text{Ni}_{10}$ at 2730 K and 250 GPa (20). More recently, an ordered bcc phase (B2) was found to coexist with the hcp phase in $\text{Fe}_{93}\text{Ni}_7$ alloy at 2970 K and 186 GPa (21). Additionally, recent ab initio molecular dynamics (AIMD) simulations have revealed an

hcp-bcc mixed structure that crystallized in $\text{Fe}_{85}\text{Ni}_{15}$ melts under IC conditions (22). However, because the simulation involved large supercooling and rapid crystallization, it remains unclear whether the hcp-bcc mixed structure is thermodynamically stable. To fully understand the crystalline structure of the IC, it is crucial to compute the Fe-Ni phase diagram, accounting for the competition among the bcc, hcp, and fcc phases and their dependence on nickel concentrations under IC conditions.

Despite its importance, theoretically exploring the stability of the Fe-Ni alloy at IC conditions is challenging. Previous ab initio calculations of Fe-Ni alloys were conducted at core pressures but at 0 K, neglecting high-temperature effects (23). Anharmonic vibrational effects at high temperatures play a critical role in the free energy and phase stability, especially for the bcc phase of iron at IC conditions. Additionally, the Fe-Ni alloy is a mixed system, meaning that ordered configurations alone cannot fully capture its free energy (7, 24, 25). For example, the stability of fcc and hcp phases in the IC is sensitive to the chemical disorder between Fe and Ni atoms (18). Static calculations have already demonstrated that certain randomly mixed Fe-Ni configurations can stabilize the dynamic behavior of the bcc phase at IC pressures (26).

Here, we use a hybrid approach that combines AIMD and Monte Carlo (MC) simulations to investigate the mixing effects of Fe and Ni in the solid phases. By calculating the ab initio mixing free energy, we construct the Fe-Ni solid-liquid phase diagram under IC conditions. This phase diagram defines the stability of various solid and liquid solutions, enabling us to identify the stable solid phases in the IC based on temperature and nickel composition.

RESULTS

Mixing enthalpy for Fe-Ni phases

To obtain the Fe-Ni phase diagram, it is essential to compute the mixing enthalpy for the nonideal solution phases under high-pressure and high-temperature conditions of IC. We supplement AIMD with additional chemical species-swapping steps using the MC algorithm to accelerate the sampling of diverse configurations (27). Figure 1A compares MC + AIMD and pure AIMD for $\text{Fe}_{90}\text{Ni}_{10}$. Both simulations were initialized with the same randomly distributed FeNi configuration in a bcc lattice. Because of the swap mechanism,

¹Department of Physics, Xiamen University, Xiamen, Fujian 361005, China. ²Department of Physics and Astronomy, Iowa State University, Ames, IA 50011, USA. ³Department of Applied Physics and Applied Mathematics, Columbia University, New York, NY 10027, USA. ⁴Department of Earth and Environmental Sciences, Columbia University, New York, NY 10027, USA. ⁵Lamont-Doherty Earth Observatory, Columbia University, Palisades, NY 10964, USA. ⁶Data Science Institute, Columbia University, New York, NY 10027, USA.

*Corresponding author. Email: yangsun@xmu.edu.cn

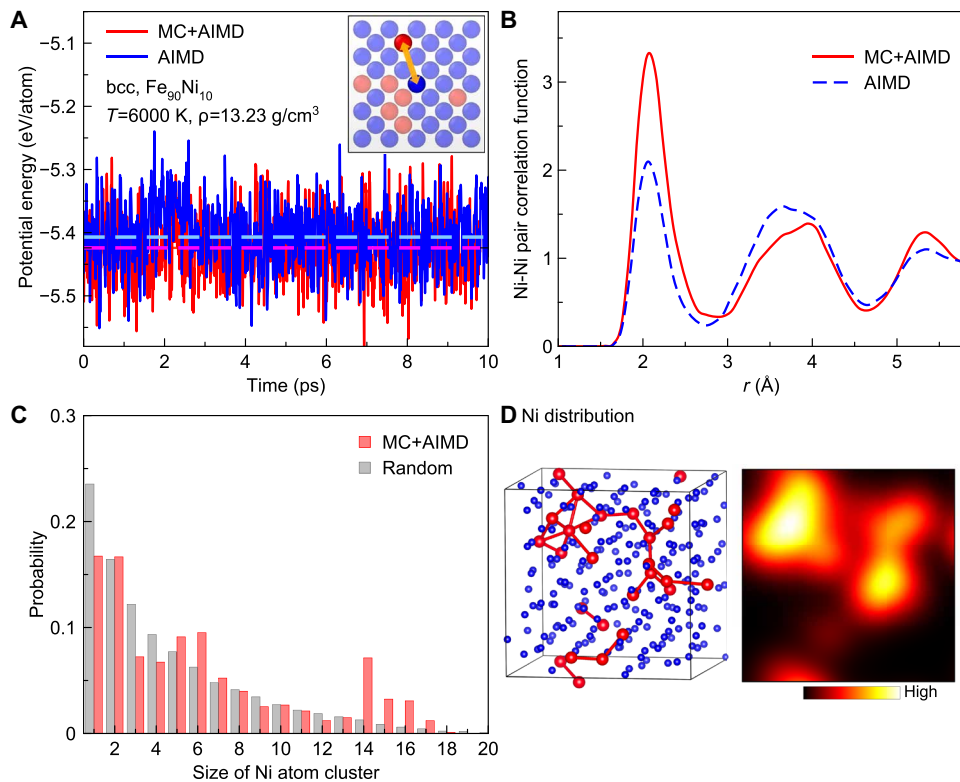


Fig. 1. MC + AIMD simulation of $\text{Fe}_{90}\text{Ni}_{10}$ solid solutions. (A) Potential energy as a function of time for $\text{Fe}_{90}\text{Ni}_{10}$ bcc phase from the MC + AIMD (red) and pure AIMD simulations (blue), starting from the same initial configuration. The simulation was carried out with fixed temperature and volume. The dashed lines are averaged potential energies for two simulations. The inset shows the schematic of the MC swap, where two atoms of different types (shown in different colors) are randomly selected and swapped to sample the configurational space, with one swap attempt highlighted by the arrow. (B) Ni-Ni pair correlation function from two simulations in (A). (C) Probabilities of Ni atoms forming different size of clusters. The statistical data of random distribution were obtained by distributing atoms randomly in the perfect lattice 10,000 times. The bond length threshold of forming a cluster is 2.9 Å, which is the first minimal of the Ni-Ni pair correlation function. (D) The left panel shows an atomic configuration with a Ni cluster of 14 atoms (longest chain) from MC + AIMD simulation. Red is Ni, while blue is Fe. The size of Fe atoms is reduced for clarity. Right panel shows the coarse-grained Ni distribution by a Gaussian smearing scheme as $D(\vec{r}) = \sum_i \left(\frac{1}{2\sigma^2\pi} \right)^{3/2} e^{-(\vec{r} - \vec{r}_i)^2/2\sigma^2}$, where \vec{r}_i is the position of Ni atoms. σ is set to 1.23 Å so that the full width at half maximum of the Gaussian function equals the first minimal of Ni-Ni pair correlation function.

the atomic configurations in MC + AIMD effectively change, approaching the low-energy states. This results in a lower averaged potential energy in the MC + AIMD simulation by 17 meV/atom compared to the one from AIMD. Statistical analysis in text S1 suggests that the error in enthalpy obtained from the MC + AIMD simulations is less than 2 meV/atom. Figure 1B shows marked structural differences between MC + AIMD and pure AIMD simulations based on the Ni-Ni pair correlation functions. Compared to the pure AIMD results, the MC + AIMD simulation leads to an enhanced first peak at 2.1 Å and a third peak at 5.3 Å in $g_{\text{Ni-Ni}}(r)$. The second peak of $g_{\text{Ni-Ni}}(r)$ is shifted toward longer distances in the MC + AIMD result. These differences suggest that the Ni-Ni pairs in the MC + AIMD simulation exhibit short- to medium-range orders rather than a random distribution. To understand the spatial orders, we connect the Ni-Ni bonds using a cutoff value of first minimal in $g_{\text{Ni-Ni}}(r)$ and analyze the size distribution of Ni clusters in Fig. 1C. Compared to the randomly distributed Ni atoms in the same lattice, the configurations sampled by MC + AIMD show a lower probability of forming isolated Ni atoms but a higher probability of forming large clusters. We plot one snapshot in Fig. 1D, which contains a large cluster of 14 Ni atoms. The Ni atoms form an

interconnected framework, leading to a nonuniform Ni distribution in the lattice, as depicted by the coarse-grained distribution in Fig. 1D. Thus, the MC + AIMD simulations demonstrate that a small amount of Ni tends to form nonideal and nonuniform solid solutions in the Fe's lattice under IC conditions.

On the basis of the hybrid MC + AIMD simulations, the mixing enthalpy can be computed for all three solid phases. To obtain the mixing enthalpy at a consistent pressure and temperature of 323 GPa and 6000 K, we perform the simulations using the canonical ensemble with three different volumes near the target pressure for each phase, shown in fig. S2. We mainly focus on the Earth's core. Figure 2A illustrates the mixing enthalpy as a function of Ni concentration for the hcp, fcc, bcc, and liquid solutions from hybrid MC + AIMD simulations at 323 GPa and 6000 K. The mixing enthalpy of the liquid phase is higher than that of all three solid phases. The bcc solution exhibits the lowest mixing enthalpy among the solid phases, while the hcp and fcc phases show similar mixing enthalpies. The mixing enthalpy of solid solutions at low Ni compositions (<10%) deviates from a typical regular solution model. In particular, the bcc solution shows a negative mixing enthalpy at 5 atomic % (at %), suggesting that mixing is

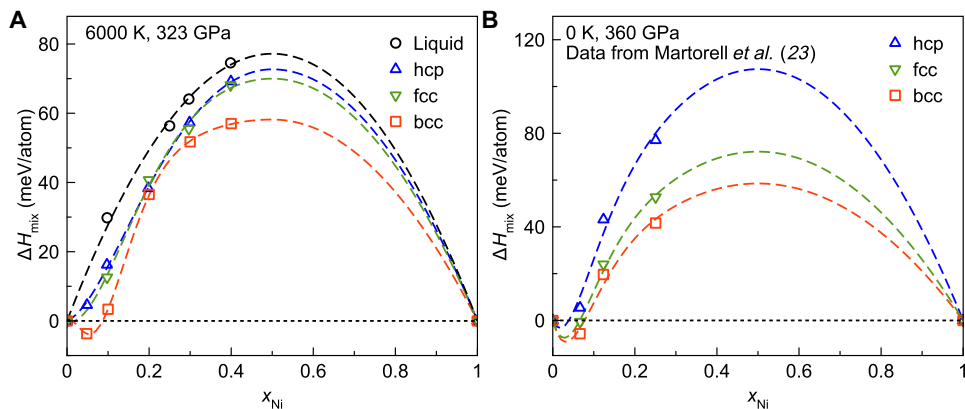


Fig. 2. Mixing enthalpy for $\text{Fe}_{1-x}\text{Ni}_x$ phases. (A) Mixing enthalpy from our simulations at 323 GPa and 6000 K. The liquid data are from direct AIMD simulations. The data of solid solutions were obtained via hybrid MC + AIMD simulations. The dashed lines are the fitting results with the RK polynomial functions. The fitting parameters are included in text S2. (B) Mixing enthalpy data at 0 K and 360 GPa from (23).

energetically more favored than pure elemental phases at low Ni compositions, even if the entropy is not considered. The Redlich-Kister (RK) polynomial functions can fit these data well with errors less than 2 meV/atom. Martorell *et al.* (23) previously examined the enthalpy of Fe-Ni alloys with static calculation at 0 K and 360 GPa. By replotting the enthalpy data from (23) using the definition in Eq. 3, similar trends can be observed in Fig. 2 (A and B), consistently showing that the bcc solution has the lowest mixing enthalpy and negative values at low Ni compositions.

Fe-Ni phase diagram

In addition to the mixing enthalpy, the Gibbs free energy of the pure end members is also crucial for the phase diagram calculations. We use the recently developed free energy methods and previous ab initio datasets (22, 24) to complete the free energy calculations of the liquid, hcp, fcc, and bcc phases for both Fe and Ni near their melting points at 323 GPa. We used the two sets of projector augmented-wave (PAW) potentials to calculate the free energy of the Fe and Ni end members, which was found to be important recently (24, 25, 28). The relative free energies with respect to (w.r.t.) the liquid phases are shown in Fig. 3 (A and B) for Fe and Ni, respectively. In the case of Fe in Fig. 3A, the hcp phase is the most stable, while fcc and bcc are metastable. Including $3s^23p^6$ electrons for Fe increases melting point by approximately 500 K but does not change the relative phase stability among hcp, fcc, and bcc phases. In the case of Ni shown in Fig. 3B, the $3s^23p^6$ electrons increase the melting point and modify the relative phase stability. Without $3s^23p^6$ electrons, hcp, fcc, and bcc phases have very similar free energies, with the bcc phase as the most stable. However, when the $3s^23p^6$ electrons are considered, the fcc phase becomes the most stable. These electrons affect the relative phase stabilities of Fe and Ni. Thus, although including $3s^23p^6$ electrons increases the computational cost by a factor of 10, they are still necessary for a comprehensive description of phase competition for pure Fe and Ni systems under the large pressures of the IC. Figure 3 (A and B) suggests that the substantially higher melting temperature of Ni compared to Fe persists with different PAW potentials, as shown earlier (22). Combining the pure free energy data and the mixing enthalpy, we can compute the Gibbs free energy of mixing in the solution model based on Eqs. 1 to 4. The

Gibbs free energy of mixing was also compared with and without contributions of $3s^23p^6$ electrons. As shown in fig. S3, including $3s^23p^6$ electrons systematically decreases the Gibbs free energy of mixing for all four phases, further stabilizing the mixture w.r.t. the decomposition. Using the liquid phase as the reference, the relative Gibbs free energy of mixing changes differently for different phases with two sets of the PAW potentials, as shown in fig. S4. Thus, including $3s^23p^6$ electrons is necessary to correctly describe the competition among Fe-Ni solutions.

The comprehensive Gibbs free energy data of Fe-Ni alloys allow us to study the phase competition under IC conditions. In Fig. 3 (C and D), we compare the Gibbs free energy among four Fe-Ni phases at 6470 K and analyze the differences between the ideal and nonideal mixing models. In the ideal mixing model shown in Fig. 3C, the liquid phase is the lowest-energy state for $0\% < x_{\text{Ni}} < 20\%$. The small Gibbs free energy differences w.r.t. the other phases of ~20 meV/atom are similar or even smaller than the mixing enthalpy differences among the four phases, making the ideal mixing model unsuitable. As shown in Fig. 3D, the nonideal mixing model dramatically changes the relative Gibbs free energies. The common tangent lines can provide phase boundaries and the equilibrium phases at different compositions. It suggests that at 6470 K and 323 GPa, the liquid phase is stable for $x_{\text{Ni}} < 2.6\%$, and the liquid and bcc phases coexist in equilibrium for $2.6\% < x_{\text{Ni}} < 4.8\%$. For $4.8\% < x_{\text{Ni}} < 12.3\%$, the bcc phase is stable; for $12.3\% < x_{\text{Ni}} < 15\%$, the bcc phase coexists with the hcp phase, and for $x_{\text{Ni}} > 15\%$, the hcp phase is the only stable phase. Therefore, the nonideality of the solid solution plays a crucial role in the phase stability of the Fe-Ni alloy at IC conditions. Besides, Fig. 3D indicates that the bcc and hcp-bcc mixtures can be stabilized at different temperatures, pressures, and compositions. We obtain the phase diagram by optimizing the free energy data w.r.t. the phase compositions at various temperatures.

Figure 4 presents $\text{Fe}_{1-x}\text{Ni}_x$ phase diagrams at 323 GPa, illustrating the phase relationships among the bcc, hcp, fcc, and liquid phases, constructed using different solution models. In both phase diagrams, the hcp phase remains the stable phase at low nickel concentrations ($x_{\text{Ni}} < 3\%$), and the addition of nickel raises the melting temperature. This phenomenon can be attributed to two factors: (i) Ni has a higher melting temperature than Fe, and (ii) the mixing

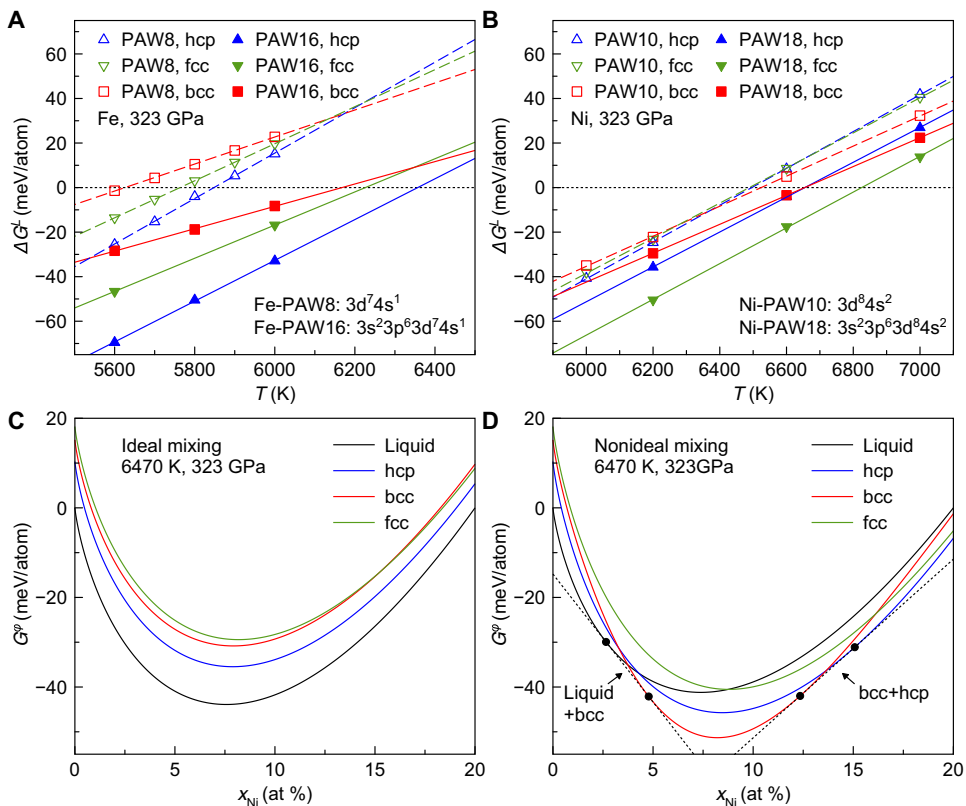


Fig. 3. Ab initio Gibbs free energy of pure and solution phases. (A) Free energy of pure Fe phases, referenced to the liquid data at 323 GPa near the melting temperatures for Fe. The bcc and hcp data are from (24). (B) Free energy of pure Ni, referenced to the liquid (L) phase at 323 GPa near the melting temperatures for Ni. The data obtained via PAW10 are from (22). (C) Free energy of Fe-Ni phases from the ideal solution model, referenced to the liquid phase at 0% and 20% Ni. (D) Free energy of Fe-Ni phases from the nonideal mixing model. The dashed lines represent the common tangent lines that define the solidus and liquidus compositions.

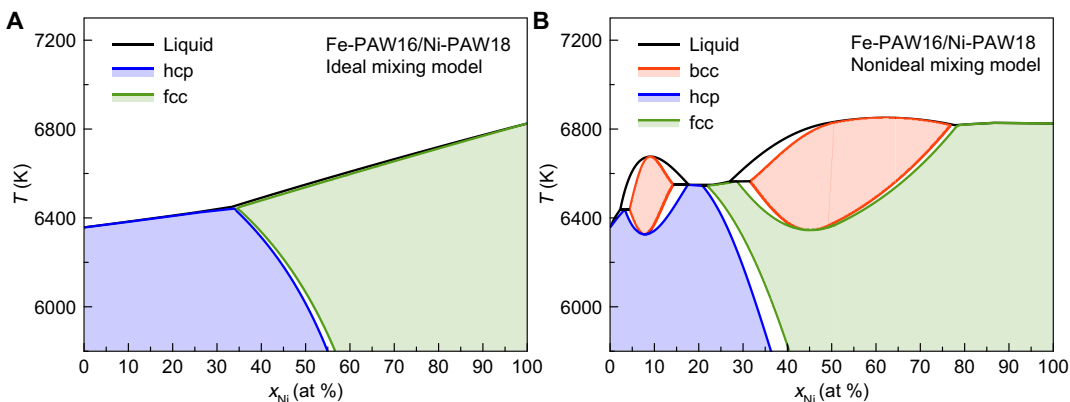


Fig. 4. Fe_{1-x}Ni_x phase diagrams at 323 GPa using different models. (A) Ideal mixing model. (B) Nonideal mixing model.

enthalpy of the liquid phase is higher than that of all solid phases, further increasing the free energy of the liquid solution relative to the solid phases. The difference between Fig. 4A and Fig. 4B indicates that the nonideal mixing stabilizes the bcc phase near the liquidus lines. The phase diagram in Fig. 4B includes the effects of $3s^23p^6$ electrons and nonideal mixing, thus providing the highest accuracy for the Fe-Ni alloy under IC conditions. It shows that the bcc phase is stable within approximately 400 K below the liquidus lines in the range of 3% to 18% and 28% to 78% Ni compositions. At

lower temperatures, the hcp phase is favored in the Fe-rich composition, while the fcc phase is stable for Ni-rich compositions. The phase diagrams without $3s^23p^6$ contributions are shown in fig. S5. There are notable differences between the phase diagrams in Fig. 4 and fig. S5 because the $3s^23p^6$ electrons largely stabilize the fcc phase for Ni-rich compositions. Nevertheless, the stability field of the bcc phase in Fe-rich compositions remains robust across different PAW potentials, as demonstrated by the comparison between Fig. 4B and fig. S5B.

These phase diagrams provide helpful information to understand previous experiments and simulations. For instance, there were failed attempts to observe the bcc phase in $\text{Fe}_{90}\text{Ni}_{10}$ alloy at 340 GPa and 4700 K (29). On the basis of the phase diagram in Fig. 4B, temperatures above 6300 K are required at 323 GPa to observe the bcc phase. Thus, 4700 K is still too low to observe the bcc phase near 340 GPa. The bcc phase crystallized in previous AIMD simulation with PAW10 potential for Ni at 5000 K and 323 GPa (22). However, in fig. S5A, only the hcp phase is stable in this region. The crystallization observed in (22) is attributed to the notably high nucleation rate of the metastable bcc phase, suggesting that Ni likely follows a two-step nucleation mechanism, i.e., the metastable phase forms initially in the nucleation process, as observed for Fe under IC conditions (30). The phase diagram in Fig. 4 also helps explain the mixed hcp-bcc phase crystallized in $\text{Fe}_{85}\text{Ni}_{15}$ alloy (22). With 15% Ni, the phase diagram shows a stable region of hcp-bcc coexistence at \sim 6000 K. Under 310 GPa and 5000 K conditions used in (22), while the hcp phase should be the stable phase for the $\text{Fe}_{85}\text{Ni}_{15}$ alloy, the bcc phase will likely have a higher nucleation rate to start the crystallization. Therefore, the system starts the nucleation process with the bcc phase and grows an hcp-bcc mixture to reduce the free energy. Such a mixture should also be a metastable phase, promoting the crystallization process, and could be the intermediate phase of two-step nucleation for the $\text{Fe}_{85}\text{Ni}_{15}$ alloy under IC conditions.

There are still limitations in present phase diagram calculations. The length scale in our current MC + AIMD simulations is restricted by the computational resources required for ab initio calculations. While the statistical error in enthalpy calculations was analyzed as insignificant, it remains unclear whether pronounced medium-range ordering could emerge in larger-scale simulations (31, 32). Additionally, the mixing entropy in the solution model is the same as in the ideal solution model, disregarding the nonideal effect on the mixing entropy and vibrational entropy changes arising from alloying (33, 34). To evaluate the effect of these limitations, we developed a semi-empirical Fe-Ni potential to study the phase diagram, as described in text S4. On the basis of the interatomic potential, the mixing effects between Fe and Ni can be accurately considered with large simulation cells, accurate semi-grand canonical MC, and solid-liquid coexistence simulations. As shown in fig. S12, these effects can introduce uncertainties of \sim 2 at % and 100 K for the current phase boundary at $x_{\text{Ni}} = 10$ at %, assuming that the error propagates similarly in classical and ab initio systems. The results obtained with the semi-empirical potential indicate that our solution model effectively captures the main features of the phase diagram. On the other hand, while the free energy of the $\text{Fe}_{1-x}\text{Ni}_x$ alloy can be accurately computed at the classical level, the semi-empirical potential still cannot fully reproduce the ab initio enthalpy of mixing accurately for x_{Ni} larger than 15%. This highlights the need for a Fe-Ni interatomic potential with ab initio accuracy suitable for IC conditions. The recent development of deep-learning techniques could provide a feasible approach to addressing such issues in future studies (28, 35).

Potential consequences for the IC structure

On the basis of the Fe-Ni phase diagram (Fig. 4B) and disregarding the effects of light elements for the moment, we can ponder on the effect of Ni on the present IC structure, assuming that it is in thermochemical equilibrium everywhere. There is a complex competition between hcp, bcc, and their mixtures as shown Fig. 4B, specifically at $5\% < x_{\text{Ni}} < 15\%$, which corresponds to the composition range

relevant to the core based on the Ni content observed in chondritic and iron meteorites (36, 37). On the basis of the current understanding of the core's thermal structure (38), the temperature at the IC boundary (ICB) is at the intersection of liquidus line of core materials and the liquid core adiabat. The IC should be isothermal due to its large thermal conductivity (38, 39). The pressure increase toward the IC center (ICC) should raise the liquidus temperature of the alloy. Here, we assume that this increase in liquidus temperature, ΔT , is similar to the increase in melting temperature of Fe with pressure, i.e., approximately 200 to 300 K from 330 to 360 GPa (24, 40). As indicated in Fig. 5 (B and C), the multiphase equilibrium state changes with varying ΔT , i.e., depth and initial alloy composition, forming a multilayer solid core. For estimated compositions $5\% < x_{\text{Ni}} < 15\%$, we show the inferred IC structures in Fig. 5C. If $x_{\text{Ni}} = 5\%$, one should expect a large range of liquid + bcc mixture near the ICB. With increasing depth, a layer of pure bcc phase stabilizes, and a mixture of hcp + bcc phases stabilizes at the center. Small changes in x_{Ni} can change the thickness of these layers. If $x_{\text{Ni}} = 10\%$, the liquid + bcc layer near the ICB becomes relatively thinner, with only a single bcc phase in the IC. If $x_{\text{Ni}} = 15\%$, the pure bcc phase domain should disappear, and a pure hcp phase should emerge at the ICC. The phase diagram in Fig. 5B suggests that a liquid + bcc mixture at the ICB should always exist for $5\% < x_{\text{Ni}} < 15\%$, as shown in Fig. 5C. However, the solid structure in the IC is sensitive to the Ni concentration. Within this alloy concentration range, the bcc phase always exists somewhere, while the hcp phase may not (as in scenario 2). The hcp phase becomes the only solid phase for $x_{\text{Ni}} < 3\%$ or $x_{\text{Ni}} > 18\%$.

The IC structure deduced from the Fe-Ni phase diagram is, therefore, much more complex than the typical structure derived from pure Fe. The proposed multilayer structure model might be the origin of some seismic anomalies (41–44). Future analysis of sound velocity in the multiphase mixture of the FeNi system is crucial for revealing its correlation with seismological evidence (45–47). Since the phase diagram of the Fe-Ni alloy is quite different from that of pure Fe at relevant conditions, the presence of Ni in the core might affect the current understanding of light element partitioning between IC and OC (8). In turn, these light elements may also influence phase stability. For instance, silicon has been shown to stabilize the ordered bcc phase (B2) in the Fe-Ni alloy (21), while high hydrogen concentrations can stabilize the fcc phase (48). Thus, the effects of other light elements on the phase stability must be considered together with the Fe-Ni phase diagram to fully understand the core's structure. The Fe-Ni alloy's distinct crystallization kinetics may also provide different insights into the IC formation and evolution (30, 49, 50).

DISCUSSION

Using nonideal mixing models, we computed the ab initio phase diagram of the Fe-Ni system under IC conditions. We used a hybrid MC + AIMD simulation to explore different configurations of $\text{Fe}_{1-x}\text{Ni}_x$ solid solutions, a task that is not feasible with conventional AIMD. The simulation reveals that Ni atoms cluster and form nonideal and nonuniform solid solutions with Fe at core conditions. By comparing phase diagrams computed with different accuracy levels, we demonstrate that the effect of $3s^23p^6$ electrons and nonideal mixing are critical for accurately determining the Fe-Ni phase diagram at core conditions. At 323 GPa and $4\% < x_{\text{Ni}} < 18\%$ or $28\% < x_{\text{Ni}} < 78\%$, the bcc phase is the stable phase for temperatures down to \sim 400 K

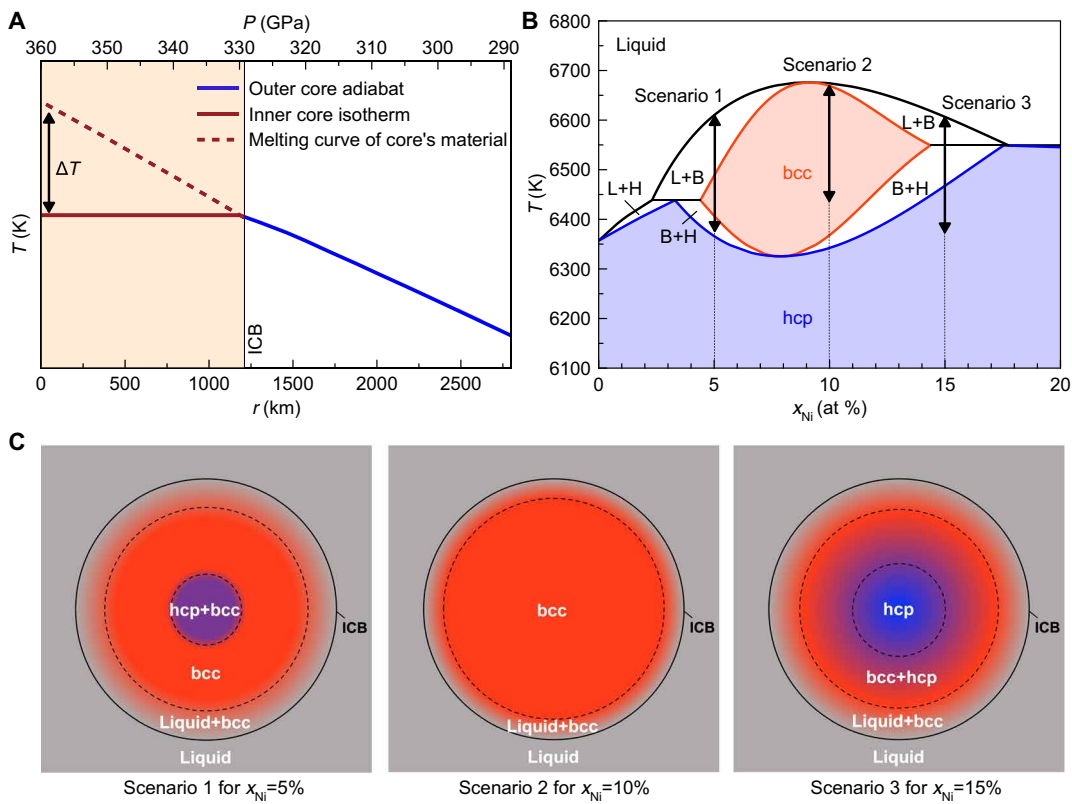


Fig. 5. IC structure implied by the Fe-Ni phase diagram. (A) Schematic of core's thermal structure. OC adiabats are anchored to the melting curve of the core's material at the ICB. The IC is approximated as isothermal (38, 39). The arrow indicates the temperature difference between the core material's melting point and the IC's temperature. (B) Fe-Ni phase diagram for Fe-rich compositions relevant to the IC. The arrow indicates a temperature span of 250 K from the ICB to the ICC at three different Ni compositions. (C) Different IC structures based on the stable phases at Ni compositions of 5%, 10%, and 15%, deduced from the phase diagram in (B).

below the liquidus line. At lower temperatures, the hcp phase is stable in Fe-rich compositions, while the fcc phase is stable in Ni-rich compositions. The phase diagram provides useful insights for understanding previous experimental observations and crystallization simulation for the Fe-Ni alloy under core conditions. It also suggests scenarios for IC structures far more complex than usually assumed with pure Fe phases. The ICB should exhibit liquid-bcc coexistence. The IC can have multiple layers composed of hcp, bcc, and their mixture, which highly depends on the Ni's composition. The present study emphasizes the crucial effect of Ni on the IC structure. It also paves the way for future calculations of thermodynamic properties of multicomponent systems with Fe, Ni, and light elements.

MATERIALS AND METHODS

Ab initio molecular dynamics and swap MC simulation

Ab initio calculations were performed with the Vienna ab initio simulation package (VASP) (51). The electron-ion interaction was described using the PAW method (52), and the exchange-correlation energy was treated with the generalized gradient approximation (GGA) in the Perdew-Burke-Ernzerhof (PBE) form (53). The electronic entropy was described by the Mermin functional (54, 55). The electronic temperature in the Mermin functional is kept the same as the ionic temperature. Two sets of PAW-PBE potentials were used for AIMD and MC simulations: PAW8 with 3d⁷4s¹ valence electrons for Fe and PAW10 with 3d⁸4s² for Ni. PAW16 with 3s²3p⁶3d⁷4s¹ valence electrons for Fe and PAW18 with 3s²3p⁶3d⁸4s² for Ni were also used to improve the density functional theory (DFT) accuracy via thermodynamic integration and free energy perturbation (FEP) (see text S3) (24, 25, 56). The plane-wave cutoff energies were set to 400 eV for PAW8/PAW10 and 750 eV for PAW16/PAW18. Supercells containing 288, 250, 256, and 256 atoms were used for the hcp, bcc, fcc, and liquid phases, respectively. The Γ point was used to sample the Brillouin zone in AIMD and MC simulations. A dense Monkhorst-Pack k -point mesh of $2 \times 2 \times 2$ was adopted for all phases to achieve high DFT accuracy in the FEP calculations.

We used the MC swap algorithm for the solid phases (bcc, hcp, fcc) to sample mixing configurations of Fe-Ni solid solutions as implemented in (27). Fe and Ni atoms were randomly exchanged on the fly during the AIMD simulation. The acceptance probability of the trial swap was determined based on the Metropolis algorithm with the probability of $\min[1, \exp(-\Delta E/k_B T)]$, where ΔE represents the total energy change due to the swap. One swap was attempted every 100 AIMD steps with approximately 80% acceptance rates on average. The atomic forces were updated for the configuration after the accepted swap. Kinetic energy was conserved during the swaps by scaling the velocities of the swapped atoms according to the ratio of their masses. Enthalpies were directly obtained from the ab initio total energies for the ensemble average. The Nosé-Hoover thermostat (57) was used to control the temperature, and a time step

of 1.0 fs was used to integrate Newton's equations of motion in the AIMD simulations. This hybrid approach can substantially accelerate the equilibration process and enhance the configurational diversity of the simulated ensemble for solid solutions (27, 58, 59).

Phase diagram of binary solutions

For completeness, we briefly review the thermodynamics of binary systems for phase diagram construction. When Fe and Ni are mixed to form a solution phase φ at constant temperature and pressure, the change in Gibbs free energy during mixing, referred to as the Gibbs free energy of mixing, is expressed as

$$\Delta G_{\text{mix}}^{\varphi} = \Delta H_{\text{mix}}^{\varphi} - T \Delta S_{\text{mix}}^{\varphi} \quad (1)$$

where $\Delta H_{\text{mix}}^{\varphi}$ is the mixing enthalpy and $\Delta S_{\text{mix}}^{\varphi}$ is the mixing entropy. In an ideal solution model, $\Delta H_{\text{mix}}^{\varphi} = 0$ and the entropy of mixing is given by

$$\Delta S_{\text{mix}}^{\varphi} = -k_B T [x \ln x + (1-x) \ln (1-x)] \quad (2)$$

where k_B is the Boltzmann constant and x is the composition of nickel. In a nonideal solution, $\Delta H_{\text{mix}}^{\varphi} \neq 0$. Therefore, a solution model with nonideal mixing enthalpy is needed (60), represented as

$$\Delta H_{\text{mix}}^{\varphi} = H_{\text{Fe}_{1-x}\text{Ni}_x}^{\varphi} - (1-x)H_{\text{Fe}}^{\varphi} - xH_{\text{Ni}}^{\varphi} \quad (3)$$

where H_{Fe}^{φ} and H_{Ni}^{φ} are the enthalpy of pure Fe and Ni in phase φ . The configurational entropy is approximated using the ideal mixing entropy. This model provides a first-order approximation of a nonideal solution, given that Fe and Ni atoms have similar sizes and the mixing enthalpy deviates from the ideal solution by only a few meV/atom at low Ni concentrations. As long as $\Delta H_{\text{mix}}^{\varphi}$ is calculated accurately, this solution model can capture the detailed features of the phase diagram and phase competitions effectively (61–63). The Gibbs free energy for the solution phase is

$$G^{\varphi}(x, T, P) = \Delta G_{\text{mix}}^{\varphi} + (1-x)G_{\text{Fe}}^{\varphi} + xG_{\text{Ni}}^{\varphi} \quad (4)$$

where G_{Fe}^{φ} and G_{Ni}^{φ} are the free energy of pure Fe and Ni, respectively. φ denotes the liquid, hcp, fcc, or bcc phase in this study.

The binary phase diagram of a multiphase mixture is determined by minimizing the total Gibbs free energy of the assemblage. This process can be effectively addressed using the CALPHAD (calculation of phase diagrams) approach (64). The Gibbs free energy data of different Fe-Ni phases computed from the first-principles simulations were fitted with the RK expression (65) as

$$G^{\varphi}(x, T, P) = \sum_{i=\text{Fe},\text{Ni}} x_i G_i^{\varphi} + k_B T \sum_i x_i \ln x_i + x_{\text{Fe}} x_{\text{Ni}} \sum_{\varphi=0}^n L_{\varphi}^v (x_{\text{Fe}} - x_{\text{Ni}})^v \quad (5)$$

where L_{φ}^v are the fitting parameters. The multiphase free energy minimization was solved by computing the convex hull via the Py-Calphad software (66).

Supplementary Materials

This PDF file includes:

Texts S1 to S4

Figs. S1 to S12

Table S1

References

REFERENCES AND NOTES

1. F. Birch, Elasticity and constitution of the Earth's interior. *J. Geophys. Res.* **57**, 227–286 (1952).
2. K. Hirose, S. Labrosse, J. Hernlund, Composition and state of the core. *Annu. Rev. Earth Planet. Sci.* **41**, 657–691 (2013).
3. O. L. Anderson, Properties of iron at the Earth's core conditions. *Geophys. J. Int.* **84**, 561–579 (1986).
4. G. Steinle-Neumann, L. Stixrude, R. E. Cohen, O. Güleren, Elasticity of iron at the temperature of the Earth's inner core. *Nature* **413**, 57–60 (2001).
5. Y. Zhang, Y. Wang, Y. Huang, J. Wang, Z. Liang, L. Hao, Z. Gao, J. Li, Q. Wu, H. Zhang, Y. Liu, J. Sun, J.-F. Lin, Collective motion in hcp-Fe at Earth's inner core conditions. *Proc. Natl. Acad. Sci. U.S.A.* **120**, e2309952120 (2023).
6. L. Vočádlo, I. G. Wood, M. J. Gillan, J. Brodholt, D. P. Dobson, G. D. Price, D. Alfè, The stability of bcc-Fe at high pressures and temperatures with respect to tetragonal strain. *Phys. Earth Planet. Inter.* **170**, 52–59 (2008).
7. A. B. Belonoshko, T. Lukinov, J. Fu, J. Zhao, S. Davis, S. I. Simak, Stabilization of body-centred cubic iron under inner-core conditions. *Nat. Geosci.* **10**, 312–316 (2017).
8. K. Hirose, B. Wood, L. Vočádlo, Light elements in the Earth's core. *Nat. Rev. Earth Environ.* **2**, 645–658 (2021).
9. J. Liu, Y. Sun, C. Lv, F. Zhang, S. Fu, V. B. Prakapenka, C. Wang, K. Ho, J. Lin, R. M. Wentzcovitch, Iron-rich Fe-O compounds at Earth's core pressures. *Innovation* **4**, 100354 (2023).
10. Y. Tian, P. Zhang, W. Zhang, X. Feng, S. A. T. Redfern, H. Liu, Iron alloys of volatile elements in the deep Earth's interior. *Nat. Commun.* **15**, 3320 (2024).
11. T. Liu, Z. Jing, Hydrogen and silicon are the preferred light elements in Earth's core. *Commun. Earth Environ.* **5**, 1–8 (2024).
12. F. Sakai, K. Hirose, G. Morard, Partitioning of silicon and sulfur between solid and liquid iron under core pressures: Constraints on Earth's core composition. *Earth Planet. Sci. Lett.* **624**, 118449 (2023).
13. L. Yuan, G. Steinle-Neumann, Hydrogen distribution between the Earth's inner and outer core. *Earth Planet. Sci. Lett.* **609**, 118084 (2023).
14. V. F. Buchwald, *Handbook of Iron Meteorites. Their History, Distribution, Composition and Structure* (Arizona State University, 1975).
15. J.-F. Lin, D. L. Heinz, A. J. Campbell, J. M. Devine, W. L. Mao, G. Shen, Iron-nickel alloy in the Earth's core. *Geophys. Res. Lett.* **29**, 1–1471 (2002).
16. T. Komabayashi, Phase relations of Earth's core-forming materials. *Crystals* **11**, 581 (2021).
17. T. Komabayashi, K. Hirose, Y. Ohishi, In situ X-ray diffraction measurements of the fcc-hcp phase transition boundary of an Fe-Ni alloy in an internally heated diamond anvil cell. *Phys. Chem. Miner.* **39**, 329–338 (2012).
18. M. Ekholm, A. S. Mikhaylушкиn, S. I. Simak, B. Johansson, I. A. Abrikosov, Configurational thermodynamics of Fe-Ni alloys at Earth's core conditions. *Earth Planet. Sci. Lett.* **308**, 90–96 (2011).
19. L. Dubrovinsky, N. Dubrovinskaia, O. Narygina, I. Kantor, A. Kuznetsov, V. B. Prakapenka, L. Vitos, B. Johansson, A. S. Mikhaylушкиn, S. I. Simak, I. A. Abrikosov, Body-centered cubic iron-nickel alloy in Earth's core. *Science* **316**, 1880–1883 (2007).
20. T. Sakai, E. Ohtani, N. Hirao, Y. Ohishi, Stability field of the hcp-structure for Fe, Fe-Ni, and Fe-Ni-Si alloys up to 3 Mbar. *Geophys. Res. Lett.* **38**, 2011GL047178 (2011).
21. D. Ikuta, E. Ohtani, N. Hirao, Two-phase mixture of iron-nickel-silicon alloys in the Earth's inner core. *Commun. Earth Environ.* **2**, 225 (2021).
22. Y. Sun, M. I. Mendelev, F. Zhang, X. Liu, B. Da, C.-Z. Wang, R. M. Wentzcovitch, K.-M. Ho, Unveiling the effect of Ni on the formation and structure of Earth's inner core. *Proc. Natl. Acad. Sci. U.S.A.* **121**, e2316477121 (2024).
23. B. Martorell, J. Brodholt, I. G. Wood, L. Vočádlo, The effect of nickel on the properties of iron at the conditions of Earth's inner core: Ab initio calculations of seismic wave velocities of Fe-Ni alloys. *Earth Planet. Sci. Lett.* **365**, 143–151 (2013).
24. Y. Sun, M. I. Mendelev, F. Zhang, X. Liu, B. Da, C. Wang, R. M. Wentzcovitch, K. Ho, Ab initio melting temperatures of Bcc and Hcp iron under the Earth's inner core condition. *Geophys. Res. Lett.* **50**, e2022GL102447 (2023).
25. T. Sun, J. P. Brodholt, Y. Li, L. Vočádlo, Melting properties from ab initio free energy calculations: Iron at the Earth's inner-core boundary. *Phys. Rev. B* **98**, 224301 (2018).
26. S. Chatterjee, S. Ghosh, T. Saha-Dasgupta, Ni doping: A viable route to make body-centered-cubic Fe stable at Earth's inner core. *Minerals* **11**, 258 (2021).
27. M. Widom, W. P. Huhn, S. Maiti, W. Steurer, Hybrid Monte Carlo/molecular dynamics simulation of a refractory metal high entropy alloy. *Metall. Mater. Trans. A* **45**, 196–200 (2014).
28. F. Wu, S. Wu, C.-Z. Wang, K.-M. Ho, R. Wentzcovitch, Y. Sun, Melting temperature of iron under the Earth's inner core condition from deep machine learning. *Geosci. Front.* **15**, 101925 (2024).
29. S. Tateno, K. Hirose, T. Komabayashi, H. Ozawa, Y. Ohishi, The structure of Fe-Ni alloy in Earth's inner core. *Geophys. Res. Lett.* **39**, 2–5 (2012).

30. Y. Sun, F. Zhang, M. I. Mendelev, R. M. Wentzcovitch, K.-M. Ho, Two-step nucleation of the Earth's inner core. *Proc. Natl. Acad. Sci. U.S.A.* **119**, e2113059119 (2022).
31. J. Wang, P. Jiang, F. Yuan, X. Wu, Chemical medium-range order in a medium-entropy alloy. *Nat. Commun.* **13**, 1021 (2022).
32. Z. An, T. Yang, C. Shi, S. Mao, L. Wang, A. Li, W. Li, X. Xue, M. Sun, Y. Bai, Y. He, F. Ren, Z. Lu, M. Yan, Y. Ren, C.-T. Liu, Z. Zhang, X. Han, Negative enthalpy alloys and local chemical ordering: A concept and route leading to synergy of strength and ductility. *Natl. Sci. Rev.* **11**, nwae026 (2024).
33. A. van de Walle, G. Ceder, The effect of lattice vibrations on substitutional alloy thermodynamics. *Rev. Mod. Phys.* **74**, 11–45 (2002).
34. R. M. Wentzcovitch, J. F. Justo, Z. Wu, C. R. S. da Silva, D. A. Yuen, D. Kohlstedt, Anomalous compressibility of ferropericlase throughout the iron spin cross-over. *Proc. Natl. Acad. Sci. U.S.A.* **106**, 8447–8452 (2009).
35. F. Wu, Y. Sun, T. Wan, S. Wu, R. M. Wentzcovitch, Deep-learning-based prediction of the tetragonal → cubic transition in daveamite. *Geophys. Res. Lett.* **51**, e2023GL108012 (2024).
36. E. R. D. Scott, J. T. Wasson, Classification and properties of iron meteorites. *Rev. Geophys.* **13**, 527–546 (1975).
37. K. Łuszczek, T. A. Przylibski, Selected metal resources on H chondrite parent bodies. *Planet. Space Sci.* **206**, 105309 (2021).
38. R. A. Fischer, "Melting of Fe alloys and the thermal structure of the core" in *Deep Earth: Physics and Chemistry of the Lower Mantle and Core* (Geophysical Monograph Series, Wiley, 2016), pp. 1–12.
39. M. Pozzo, C. Davies, D. Gubbins, D. Alfè, Thermal and electrical conductivity of solid iron and iron–silicon mixtures at Earth's core conditions. *Earth Planet. Sci. Lett.* **393**, 159–164 (2014).
40. D. Alfè, G. D. Price, M. J. Gillan, Iron under Earth's core conditions: Liquid-state thermodynamics and high-pressure melting curve from ab initio calculations. *Phys. Rev. B* **65**, 165118 (2002).
41. H. Tkalčić, Complex inner core of the Earth: The last frontier of global seismology. *Rev. Geophys.* **53**, 59–94 (2015).
42. D. Tian, L. Wen, Seismological evidence for a localized mushy zone at the Earth's inner core boundary. *Nat. Commun.* **8**, 165 (2017).
43. B. Zhang, S. Ni, W. Wu, Z. Shen, W. Wang, D. Sun, Z. Wu, Small-scale layered structures at the inner core boundary. *Nat. Commun.* **14**, 6362 (2023).
44. G. Pang, K. D. Koper, S.-M. Wu, W. Wang, M. Lasbleis, G. Euler, Enhanced inner core fine-scale heterogeneity towards Earth's centre. *Nature* **620**, 570–575 (2023).
45. A. Morelli, A. M. Dziewonski, J. H. Woodhouse, Anisotropy of the inner core inferred from PKIKP travel times. *Geophys. Res. Lett.* **13**, 1545–1548 (1986).
46. M. Ishii, A. M. Dziewoński, The innermost inner core of the earth: Evidence for a change in anisotropic behavior at the radius of about 300 km. *Proc. Natl. Acad. Sci. U.S.A.* **99**, 14026–14030 (2002).
47. J. Stephenson, H. Tkalčić, M. Cambridge, Evidence for the innermost inner core: Robust parameter search for radially varying anisotropy using the neighborhood algorithm. *J. Geophys. Res. Solid Earth* **126**, e2020JB020545 (2021).
48. H. Yang, P. Dou, T. Xiao, Y. Li, J. M. R. Muir, F. Zhang, The geophysical properties of FeHx phases under inner core conditions. *Geophys. Res. Lett.* **50**, e2023GL104493 (2023).
49. L. Huguet, J. A. Van Orman, S. A. Hauck, M. A. Willard, Earth's inner core nucleation paradox. *Earth Planet. Sci. Lett.* **487**, 9–20 (2018).
50. A. J. Wilson, D. Alfè, A. M. Walker, C. J. Davies, Can homogeneous nucleation resolve the inner core nucleation paradox? *Earth Planet. Sci. Lett.* **614**, 118176 (2023).
51. G. Kresse, J. Furthmüller, Efficient iterative schemes for *ab initio* total-energy calculations using a plane-wave basis set. *Phys. Rev. B* **54**, 11169–11186 (1996).
52. P. E. Blöchl, Projector augmented-wave method. *Phys. Rev. B* **50**, 17953–17979 (1994).
53. J. P. Perdew, K. Burke, M. Ernzerhof, Generalized gradient approximation made simple. *Phys. Rev. Lett.* **77**, 3865–3868 (1996).
54. N. D. Mermin, Thermal properties of the inhomogeneous electron gas. *Phys. Rev.* **137**, A1441–A1443 (1965).
55. R. M. Wentzcovitch, J. L. Martins, P. B. Allen, Energy versus free-energy conservation in first-principles molecular dynamics. *Phys. Rev. B* **45**, 11372–11374 (1992).
56. R. W. Zwanzig, High-temperature equation of state by a perturbation method. I. Nonpolar gases. *J. Chem. Phys.* **22**, 1420–1426 (1954).
57. S. Nosé, A unified formulation of the constant temperature molecular dynamics methods. *J. Chem. Phys.* **81**, 511–519 (1984).
58. Z. Zhang, G. Csányi, D. Alfè, Partitioning of sulfur between solid and liquid iron under Earth's core conditions: Constraints from atomistic simulations with machine learning potentials. *Geochim. Cosmochim. Acta* **291**, 5–18 (2020).
59. Y. Huang, M. Widom, M. C. Gao, Ab initio free energies of liquid metal alloys: Application to the phase diagrams of Li-Na and K-Na. *Phys. Rev. Mater.* **6**, 013802 (2022).
60. D. R. Gaskell, D. E. Laughlin, *Introduction to the Thermodynamics of Materials* (CRC Press, 2017).
61. L. Kaufman, H. Bernstein, *Computer Calculation of Phase Diagrams* (Academic Press, 1970).
62. M. C. Troparevsky, J. R. Morris, P. R. C. Kent, A. R. Lupini, G. M. Stocks, Criteria for predicting the formation of single-phase high-entropy alloys. *Phys. Rev. X* **5**, 011041 (2015).
63. C. Brooks, S. Lany, Heterostructural alloy phase diagram for $(\text{Cd}_{1-x}\text{Zn}_x)_3\text{As}_2$. *Phys. Rev. Mater.* **8**, L061201 (2024).
64. P. J. Spencer, A brief history of CALPHAD. *CAL* **32**, 1–8 (2008).
65. O. Redlich, A. T. Kister, Algebraic representation of thermodynamic properties and the classification of solutions. *Ind. Eng. Chem.* **40**, 345–348 (1948).
66. R. Otis, Z.-K. Liu, pycalphad: CALPHAD-based computational thermodynamics in Python. *J. Open Res. Softw.* **5**, 1 (2017).
67. M. W. Finniss, J. E. Sinclair, A simple empirical N-body potential for transition metals. *Philos. Mag. A* **50**, 45–55 (1984).
68. M. I. Mendelev, D. J. Srolovitz, Determination of alloy interatomic potentials from liquid-state diffraction data. *Phys. Rev. B* **66**, 014205 (2002).
69. A. P. Thompson, H. M. Aktulga, R. Berger, D. S. Bolintineanu, W. M. Brown, P. S. Crozier, P. J. in't Veld, A. Kohlmeyer, S. G. Moore, T. D. Nguyen, R. Shan, M. J. Stevens, J. Tranchida, C. Trott, S. J. Plimpton, LAMMPS—A flexible simulation tool for particle-based materials modeling at the atomic, meso, and continuum scales. *Comput. Phys. Commun.* **271**, 108171 (2022).
70. B. Sadigh, P. Erhart, A. Stukowski, A. Caro, E. Martinez, L. Zepeda-Ruiz, Scalable parallel Monte Carlo algorithm for atomistic simulations of precipitation in alloys. *Phys. Rev. B* **85**, 184203 (2012).
71. D. A. Kofke, E. D. Glandt, Monte Carlo simulation of multicomponent equilibria in a semigrand canonical ensemble. *Mol. Phys.* **64**, 1105–1131 (1988).

Downloaded from https://www.science.org at Xiamen University on June 05, 2025

Acknowledgments: We thank S. Fang and T. Wu from the Information and Network Center of Xiamen University for help with graphics processing unit computing. **Funding:** Work at Xiamen University was supported by National Natural Science Foundation of China grants T2422016 and 42374108 (to Y.S.). R.M.W. acknowledges support from the Gordon and Betty Moore Foundation award GBMF12801 (doi.org/10.37807/GBMF12801) and US National Science Foundation grants EAR-2000850 and EAR-1918126 (to R.M.W.). K.-M.H. acknowledges support from US National Science Foundation grant EAR-1918134 (to K.-M.H.). The supercomputing time was partly supported by the Opening Project of the Joint Laboratory for Planetary Science and Supercomputing, Research Center for Planetary Science, and the National Supercomputing Center in Chengdu with grant no. CSYJGS-QT-2024-15 (to Y.S.).

Author contributions: Conceptualization: Y.S. Methodology: L.W., Y.S., and R.M.W. Investigation: L.W., Z.W., Y.S., R.M.W., and K.-M.H. Visualization: L.W. and Y.S. Supervision: Y.S. Writing—original draft: L.W. and Y.S. Writing—review and editing: Y.S., R.M.W., and K.-M.H.

Competing interests: The authors declare that they have no competing interests. **Data and materials availability:** All data needed to evaluate the conclusions in the paper are present in the paper and/or the Supplementary Materials.

Submitted 1 November 2024

Accepted 30 April 2025

Published 4 June 2025

10.1126/sciadv.adu1998

Supplementary Materials for
The Fe-Ni phase diagram and the Earth's inner core structure

Liangrui Wei *et al.*

Corresponding author: Yang Sun, yangsun@xmu.edu.cn

Sci. Adv. **11**, eadu1998 (2025)
DOI: 10.1126/sciadv.adu1998

This PDF file includes:

Texts S1 to S4
Figs. S1 to S12
Table S1
References

Supplementary Text 1 | Statistical analysis for MC+AIMD

The statistical error in the enthalpy calculation from MC+AIMD simulations was analyzed at 6000 K. As shown in fig. S1, four independent MC+AIMD simulations with different initial configurations and random seeds for MC swaps were performed for the *bcc*, *hcp*, and *fcc* phases. These simulations were conducted at three different volumes, and the enthalpies at 323 GPa were obtained by interpolating the enthalpy and pressure data from these calculations. The quantities are summarized in table S1. We found that the standard errors in enthalpy from the MC+AIMD simulations are less than 2 meV/atom, which are significantly smaller than the difference in mixing enthalpy (\sim 17 meV/atom) between the *bcc* and *hcp* phases at $x_{\text{Ni}}=10$ at.%. This indicates that the enthalpy error in the MC+AIMD simulations is negligible for assessing phase competition.

Supplementary Text 2 | Fitting parameters of mixing enthalpy

The mixing enthalpy of solid phases in Fig. 2A of the main text are fitted by a few Redlich-Kister polynomials as $\Delta H_{\text{mix}} = x(1-x) \sum_{v=0}^n L^v (1-2x)^v$, where x is the composition of Ni. The fitting equations are as follows

$$\Delta H_{\text{mix}}^{\text{hcp}}(x) = \begin{cases} x(1-x)[290.786 - 69.952(1-2x)^2 - 169.793(1-2x)^4], & x < 0.5 \\ 290.786(1-x), & x > 0.5 \end{cases}, \quad (\text{S1})$$

$$\Delta H_{\text{mix}}^{\text{bcc}}(x) = \begin{cases} x(1-x) \left[\frac{232.739 - 106.887(1-2x)^2}{-3975.192(1-2x)^8 + 3762.938(1-2x)^{10}} \right], & x < 0.5 \\ 232.739x(1-x), & x > 0.5 \end{cases}, \quad (\text{S2})$$

$$\Delta H_{\text{mix}}^{\text{fcc}}(x) = \begin{cases} x(1-x)[279.984 + 31.332(1-2x)^2 - 357.920(1-2x)^4], & x < 0.5 \\ 279.984x(1-x), & x > 0.5 \end{cases}, \quad (\text{S3})$$

$$\Delta H_{\text{mix}}^{\text{liquid}}(x) = 308.753x(1-x). \quad (\text{S4})$$

Supplementary Text 3 | Free energy perturbation

The free energy perturbation (FEP) is performed to obtain the free energy of mixing with $3s^23p^6$ electron contributions. As illustrated in previous work (24, 25), the Gibbs free energy difference between two systems A and B at pressure and temperature (P, T) conditions can be computed as

$$G_A(P) - G_B(P) = F_A(V_A) - F_B(V_B) + P(V_A - V_B), \quad (\text{S5})$$

where F represents the Helmholtz free energy. V_A and V_B are the equilibrium volumes at P for systems A and B, respectively. Since $P = -\frac{\partial F}{\partial V}|_T$, one can perform thermodynamic integration via

$$F_B(V_A) - F_B(V_B) = - \int_{V_B}^{V_A} P_B(V) dV, \quad (\text{S6})$$

where $P_B(V)$ is the equation of state of the system B, which is obtained by the AIMD simulations. Combining Eqns. (S5) and (S6), one can get

$$G_A(P) - G_B(P) = F_A(V_A) - F_B(V_A) + P(V_A - V_B) - \int_{V_B}^{V_A} P_B(V) dV. \quad (\text{S7})$$

We define two terms, f_{FEP} and f_{PV} , to be computed via thermodynamic integration as

$$f_{\text{FEP}} = F_A(V_A) - F_B(V_A) = -k_B T \ln \langle \exp \left(-\frac{U_A - U_B}{k_B T} \right) \rangle_B, \quad (\text{S8})$$

$$f_{\text{PV}} = P(V_A - V_B) - \int_{V_B}^{V_A} P_B(V) dV, \quad (\text{S9})$$

where U_A and U_B are the energies of the same atomic configuration computed with the Hamiltonians of systems A and B, respectively. $\langle \cdot \rangle_B$ is the ensemble average of system B. Equation (S8) is the Zwanzig equation in the FEP algorithm (56). It is formally exact, while the convergence of the ensemble average depends on the similarity between A and B systems. In our work, system B uses PAW8(10) potentials for Fe(Ni) without $3s^23p^6$ electrons, while system A uses PAW16(18) potentials for Fe(Ni) with $3s^23p^6$ electrons. The free energy difference between two systems for $\text{Fe}_{1-x}\text{Ni}_x$ alloy in the phase φ , noted as $\Delta G_{3s^23p^6}^\varphi(x)$ can be computed with FEP as

$$\Delta G_{3s^23p^6}^\varphi(x) = G_{\text{PAW16}(18)}^\varphi(x) - G_{\text{PAW8}(10)}^\varphi(x) = f_{\text{FEP}}(x) + f_{\text{PV}}(x). \quad (\text{S10})$$

In the FEP calculations, we use the trajectory from hybrid MC+AIMD simulations without $3s^23p^6$ electron contributions and recompute the energy of random snapshots with $3s^23p^6$ electron contributions. 100 snapshots from MC+AIMD simulations were used to perform the ensemble average for f_{FEP} . The fluctuations of the energy difference between systems with and without $3s^23p^6$ electrons are in the range of 3-6 meV/atom for hcp, bcc, fcc, and liquid phases, which is much smaller than the $k_B T$ of ~ 500 meV/atom at ~ 6000 K, suggesting that the FEP method is applicable for the $\text{Fe}_{1-x}\text{Ni}_x$ systems under Earth's inner core conditions. The f_{PV} term in Eqn. (S9) depends on the curvature of the equation of state for the PAW8(10) system, which is similar among different phases. Thus its contribution to the free energy difference is almost zero, similar to the one found in the previous studies (24, 25). Note $\Delta G_{3s^23p^6}^\varphi(0)$ and $\Delta G_{3s^23p^6}^\varphi(1)$ are corrections of Gibbs free energy by including $3s^23p^6$ electron contributions for pure Fe and Ni, respectively. The $\Delta G_{3s^23p^6}^\varphi(0)$ term at 323 GPa has been computed previously in Ref. (24). All $\Delta G_{3s^23p^6}^\varphi(x)$ data are shown in fig. S6. The free energy correction for $3s^23p^6$ is almost linear from pure Fe to pure Ni. The slope of liquid, bcc and hcp phases are similar. However, the data for the fcc phase shows a

crossover with that of the hcp phase. This leads to the stabilization of the fcc phase at Ni-rich compositions.

Using $\Delta G_{3s^23p^6}^\varphi(x)$, we can derive the mixing free energy change from PAW8(10) to PAW16(18) for $\text{Fe}_{1-x}\text{Ni}_x$ systems. As illustrated in Eqn. (4) of the main text, the Gibbs free energy of phase φ can be computed as

$$G_{\text{PAW8}(10)}^\varphi(x) = \Delta G_{\text{mix,PAW8}(10)}^\varphi(x) + (1 - x)G_{\text{Fe,PAW8}}^\varphi + xG_{\text{Ni,PAW10}}^\varphi. \quad (\text{S11})$$

Here we add PAW8(10) in the subscript to note the effect of PAW-PBE potential on DFT calculations. The free energy of solutions with $3s^23p^6$ electron contributions can be computed as

$$G_{\text{PAW16}(18)}^\varphi(x) = G_{\text{PAW8}(10)}^\varphi(x) + \Delta G_{3s^23p^6}^\varphi(x). \quad (\text{S12})$$

This free energy can also be written with the free energy of mixing $\Delta G_{\text{mix,PAW16}(18)}^\varphi(x)$ as

$$G_{\text{PAW16}(18)}^\varphi(x) = \Delta G_{\text{mix,PAW16}(18)}^\varphi(x) + (1 - x)G_{\text{Fe,PAW16}}^\varphi + xG_{\text{Ni,PAW18}}^\varphi. \quad (\text{S13})$$

Combining Eqn. (S10-S12) one can obtain

$$\begin{aligned} \Delta G_{\text{mix,PAW16}(18)}^\varphi(x) &= \Delta G_{\text{mix,PAW8}(10)}^\varphi(x) + \Delta G_{3s^23p^6}^\varphi(x) - (1 - x)(G_{\text{Fe,PAW16}}^\varphi - G_{\text{Fe,PAW8}}^\varphi) - \\ &x(G_{\text{Ni,PAW18}}^\varphi - G_{\text{Ni,PAW10}}^\varphi), \end{aligned} \quad (\text{S14})$$

By replacing the terms of $G_{\text{Fe,PAW16}}^\varphi - G_{\text{Fe,PAW8}}^\varphi$ and $G_{\text{Ni,PAW18}}^\varphi - G_{\text{Ni,PAW10}}^\varphi$ with $\Delta G_{3s^23p^6}^\varphi(0)$ and $\Delta G_{3s^23p^6}^\varphi(1)$, one can see the mixing free energy of PAW16(18) potential can be computed as

$$\begin{aligned} \Delta G_{\text{mix,PAW16}(18)}^\varphi(x) &= \Delta G_{\text{mix,PAW8}(10)}^\varphi(x) + \Delta G_{3s^23p^6}^\varphi(x) - (1 - x)\Delta G_{3s^23p^6}^\varphi(0) - \\ &x\Delta G_{3s^23p^6}^\varphi(1). \end{aligned} \quad (\text{S15})$$

Supplementary Text 4 | Error analysis with Fe-Ni interatomic potential

Interatomic potential development. We develop an interatomic potential to investigate the effects of simulation size and non-ideal mixing entropy on the Fe-Ni phase diagram. Several target properties were used to develop the embedded atom method (EAM) potential in the Finnis-Sinclair form (67) for the Fe-Ni system. The first group consists of the liquid structure and Gibbs free energy of pure Fe and Ni from *ab initio* MD simulations using Fe's PAW16 and Ni's PAW18 potentials. The method to fit the pair correlation functions of the liquid is described in Ref. (68), while the method to fit the Gibbs free energy will be discussed in future publications. Examination of fig. S7(A-D) reveals that the developed EAM potential reproduces these properties from density functional theory (DFT) calculations reasonably well for pure Fe and Ni under Earth's inner core

conditions. We note that the Fe component in the current EAM potential differs significantly from the Fe EAM potential developed in Ref. (30). The current EAM potential yields melting curves consistent with those obtained from Fe-PAW16 calculations for both the hcp and bcc phases, as shown in fig. S8.

To fit the Fe-Ni interactions, we include the liquid structure of the Fe₉₀Ni₁₀ alloy from *ab initio* MD simulations, as shown in fig. S7E. Since we focus on phase competition at Fe-rich compositions relevant to Earth's core, it is essential to include the mixing enthalpy at low Ni concentrations in the potential development process. Moreover, the fcc phase disappears in the phase diagram at low nickel concentrations, as shown in Fig. 4 of the main text. Thus, we only fit the *ab initio* mixing enthalpy data of the bcc, hcp, and liquid phases at $x_{\text{Ni}} = 10$ at.%. The mixing enthalpy data in Fig. S7F suggests that the developed potential provides excellent agreement with the *ab initio* data for the hcp phase. However, it shows a lower mixing enthalpy for the liquid phase by ~ 5 meV/atom and a higher enthalpy of mixing for the bcc phase by ~ 7 meV/atom compared to *ab initio* results. Nevertheless, the potential qualitatively reproduces the relative mixing enthalpy differences among the bcc, hcp, and liquid phases. Such accuracy is sufficient to produce a FeNi phase diagram similar to the one in Fig. 5B of the main text, where bcc is stable near the liquidus line at low Ni concentrations. Therefore, the EAM potential can be used to analyze the errors in the FeNi phase diagram generated with relatively small simulation cells and the non-ideal solution model (SM).

Size effect on mixing enthalpy. To examine the effect of simulation size, we computed the mixing enthalpy for solid and liquid solutions using the developed EAM potential. The enthalpy of the solutions was obtained via hybrid Monte Carlo (MC) and molecular dynamics (MD) simulations implemented in the LAMMPS software (69, 70). The simulation settings are the same as those in our MC+AIMD simulations, with a time step of 1.0 fs , and atom swaps were attempted every 100 MD steps. The mixing enthalpies of Fe₉₀Ni₁₀ phases calculated with classical MCMD and different simulation sizes are shown in fig. S9A. When the simulation size exceeds 1,000 atoms, all the mixing enthalpy data become nearly independent of simulation size, with uncertainty within 1 meV/atom. Compared to ~ 250 atoms, the mixing enthalpy of the hcp phase increases by 4 meV/atom, that of the liquid phase increased by 2 meV/atom, while the bcc phase showed very little change (< 1 meV/atom). Thus, the error in mixing enthalpy caused by simulation size is around 2-4 meV/atom for MCMD simulation.

Considering the typical error of DFT calculations is ~ 1 meV/atom, the error from simulation size in MCMD is not significant. However, it does affect the phase diagram, as illustrated in fig. S9B. Using the mixing enthalpy from both small and large simulation sizes, we computed the phase diagram based on the non-ideal SM, similar to the approach used for the *ab initio* mixing enthalpy in the main text. Due to different size effects on hcp, bcc and liquid phases, the hcp-bcc-liquid coexistence line was shifted by approximately 70 K and 2.5 at.%. The effect of this uncertainty is similar to that identified in previous Fe melting temperature studies under similar Earth's core conditions, where a 10 meV/atom energy uncertainty can cause uncertainty in Fe's melting point of ~ 200 K(25).

Effect of non-ideal mixing entropy. Our SM uses the ideal mixing entropy for the phase diagram. To evaluate the effects of the non-ideal mixing entropy, we directly calculate the Gibbs free energy of Fe-Ni solutions using the semi-grand canonical Monte Carlo (SGCMC) algorithm implemented in LAMMPS software (69, 70). The SGCMC algorithm includes mixing contributions to both enthalpy and entropy, providing an accurate description of the Gibbs free energy of mixing for solutions (71). In an SGCMC simulation, the total number of atoms and the chemical potential difference ($\Delta\mu$) between two types of atoms are fixed. At the same time, the atomic species can be exchanged by MC operations. The $\Delta\mu$ is the gradient of the free energy with respect to the equilibrium composition, i.e., $\Delta\mu = \frac{\partial G}{\partial x}$. With SGCMC, simulations at different $\Delta\mu$ are carried out to obtain the $\Delta\mu(x)$ curve. Then, the Gibbs free energy of solutions can be obtained by integrating the $\Delta\mu(x)$ curve from the pure phase to any given composition x_0 as

$$G(x_0) = G(0) + \int_0^{x_0} \Delta\mu(x) dx, \quad (\text{S14})$$

where $G(0)$ is the Gibbs free energy of the pure phase. Here, the SGCMC simulations were performed for the hcp, bcc, and liquid phases with $\sim 7,000$ atoms and 500 ps, which were tested to be sufficient to converge the results. The Nosé-Hoover thermostat and barostat were applied to control the temperature and pressure during the SGCMC simulation.

We compare the Gibbs free energy from the non-ideal SM and SGCMC for different phases. In SGCMC simulations, the $\Delta\mu(x)$ curves are computed for the bcc, hcp, and liquid phases at 323 GPa and different temperatures. An example of $\Delta\mu(x)$ at 6350 K is shown in Fig. S10A. The Gibbs free energy of each phase is computed with Eqn. (S15). The free energy data of SM and SGCMC are both shown using the pure Fe liquid free energy data as a reference for better visualization in

fig. S10B. For all three phases, the SM shows lower Gibbs free energy than those from the SGCMC simulation. This is expected because the mixing entropy in the SM is overestimated due to the assumption of ideal mixing. The differences in mixing free energy between the SM and SGCMC at 6350 K are shown in fig. S10C for the liquid, hcp, and bcc phases. This difference is primarily due to the entropy deficit in non-ideal mixing with respect to ideal mixing. Compared to the hcp and bcc phases, the liquid has a smaller difference, suggesting that the mixing in the liquid phase is closer to an ideal model. The free energy difference caused by the non-ideal mixing entropy is nearly identical for the bcc and hcp phases, as shown in fig. S10C, resulting in the cancellation of errors in the SM for the bcc and hcp phase competition. Therefore, the Gibbs free energies of bcc and hcp in Fig. S10B show an almost parallel tie-line between the results of the SM and the SGCMC, resulting in similar hcp-bcc coexistence compositions between the SM and SGCMC in fig. S10D. The free energy change of the liquid phase differs by \sim 6 meV/atom at 10 at.% compared to those of hcp or bcc phase. Overall, the size effect and non-ideal mixing entropy contributions result in a change of \sim 2 at.% and 100 K for the hcp-bcc-liquid coexistence line between the SM and SGCMC in Fig. S10D. The shape of the phase diagram, especially the stability region of the bcc phase, remains similar.

The solid-liquid coexistence (SLC) method can directly simulate the phase equilibrium of solid and liquid solutions via MCMD simulations. To this end, a solid-liquid coexistence configuration was first constructed with \sim 106,000 Fe atoms. Ni atoms randomly replaced Fe sites in both liquid and solid parts. Thus, the Ni concentrations in the liquid and solid phases are the same at the beginning of the simulation. For the hcp-liquid SLC, the simulation was performed at 6360 K and 323 GPa, while for the bcc-liquid SLC, it was performed at 6400 K and 323 GPa. Fe and Ni atoms were randomly exchanged on the fly during the simulation. The acceptance probability of the trial swap was determined based on the Metropolis algorithm with a probability of $\min(1, \exp(-\Delta E / k_B T))$, where ΔE represents the total energy change due to the swap. One swap was attempted every 100 MD steps, with a timestep of 1 fs. The simulation ran for 5 ns, ensuring that solid-liquid equilibrium was reached. As shown in fig. S11, the average Ni concentrations in the bcc/hcp phase are higher than in the liquid phase. These equilibrated concentrations from SLC simulations are consistent with the phase boundary obtained via SGCMC simulations, as shown in Fig. S9D, with an error of less than 2%.

To summarize, the tests with the Fe-Ni interatomic potential suggest that the small simulation size (~ 250 atoms) in the MCMD simulation results in errors of 2-4 meV/atom in the mixing enthalpy calculation. This error can cause the hcp-bcc-liquid coexistence line to shift by ~ 70 K and 2.5 at.%. The SGCMC and SLC simulations provide consistent phase boundaries. The ideal mixing entropy in the SM causes a systematic error in the mixing free energy difference between solid and liquid phases. However, the effect is less significant for the hcp-bcc phase competition. We use the free energy difference in Fig. S10C to estimate these effects on the *ab initio* phase diagram in Fig. 5 of the main text, assuming that the error propagates similarly in classical and *ab initio* systems. As shown in Fig. S12, the errors due to the small simulation size in MCMD and ideal mixing entropy in SM introduce uncertainties of ~ 2 at.% and 100 K for the *ab initio* phase boundary at $x_{\text{Ni}}=10$ at.%. The shape of the phase diagram, especially the stability region of the bcc phase near the liquidus line at low Ni concentrations, remains similar. We note that the study in this section provides a qualitative evaluation of uncertainties in the *ab initio* phase diagram. It still cannot serve as a full correction of the *ab initio* phase diagram because the EAM potential shows deviations from the *ab initio* results, particularly underestimated bcc phase stability at low Ni concentrations.

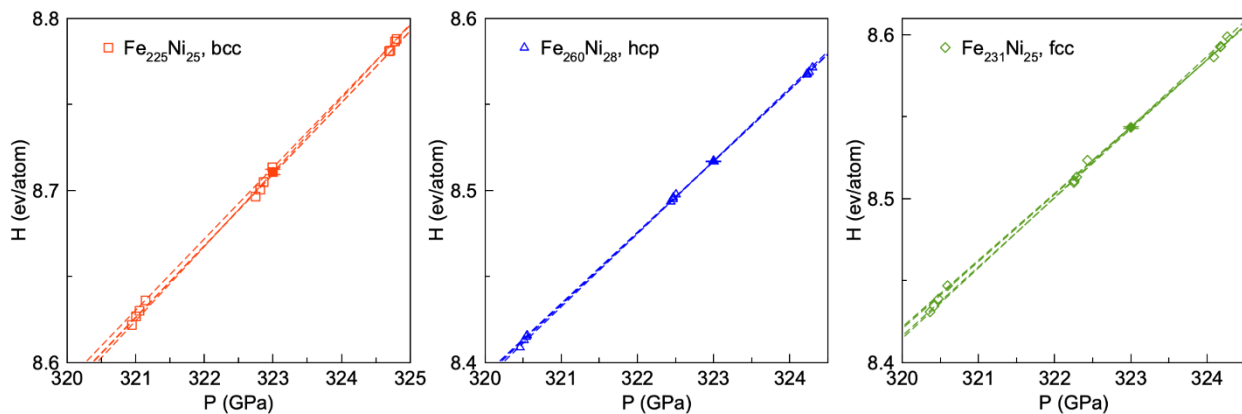


Figure S1. Enthalpy from MC+AIMD simulations. Four independent MC+AIMD simulations conducted at three different volumes for *bcc*, *hcp*, and *fcc* phases at 6000 K. The enthalpies at 323 GPa, shown by the solid symbol, were determined by interpolating the data points.

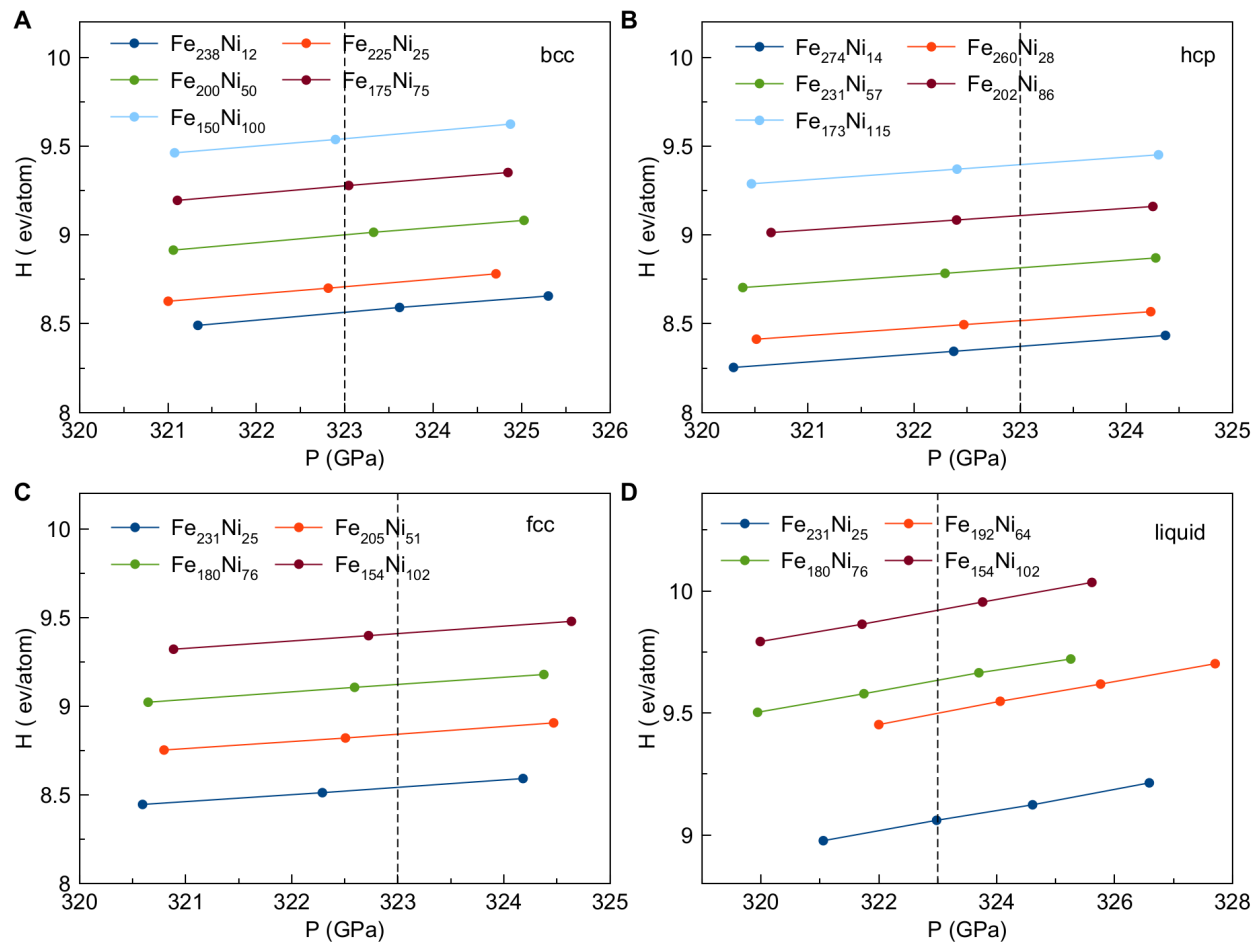


Figure S2. Enthalpy of alloys with different Ni concentrations. Pressure and enthalpy of Fe-Ni alloys with a few different volumes obtained from MC+AIMD simulations for **A.** *bcc*, **B.** *hcp*, **C.** *fcc*, and **D.** liquid phases at 6000 K. The intersection with the vertical dashed line is used to determine the enthalpy at 323 GPa.

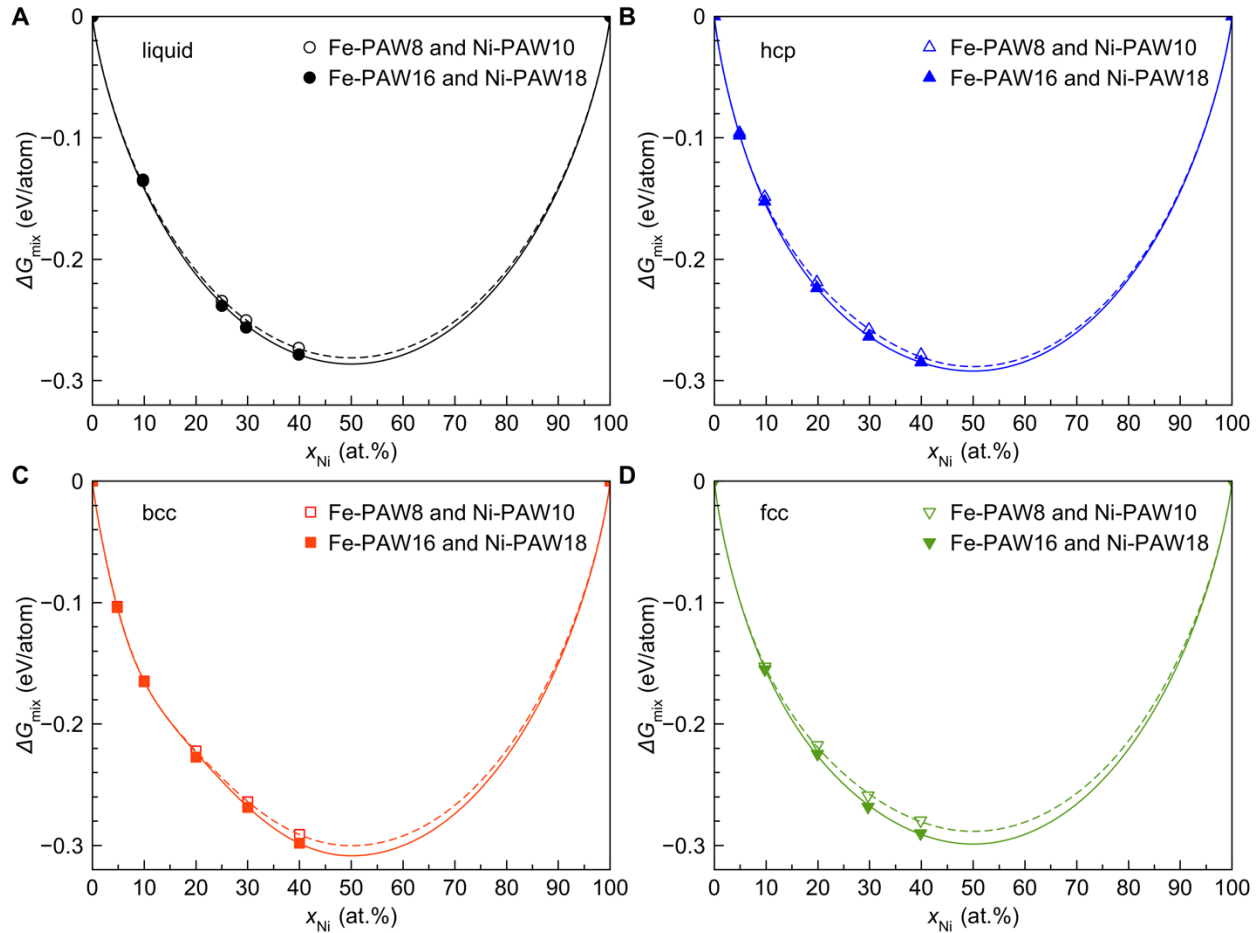


Figure S3. The Gibbs free energy of mixing. The Gibbs free energy of mixing using high-efficiency calculations (Fe-PAW8, Ni-PAW10, and Γ k-point) and high-accuracy calculations (Fe-PAW16, Ni-PAW18, and $2 \times 2 \times 2$ k-point mesh) for **A.** liquid, **B.** hcp, **C.** bcc, **D.** fcc.

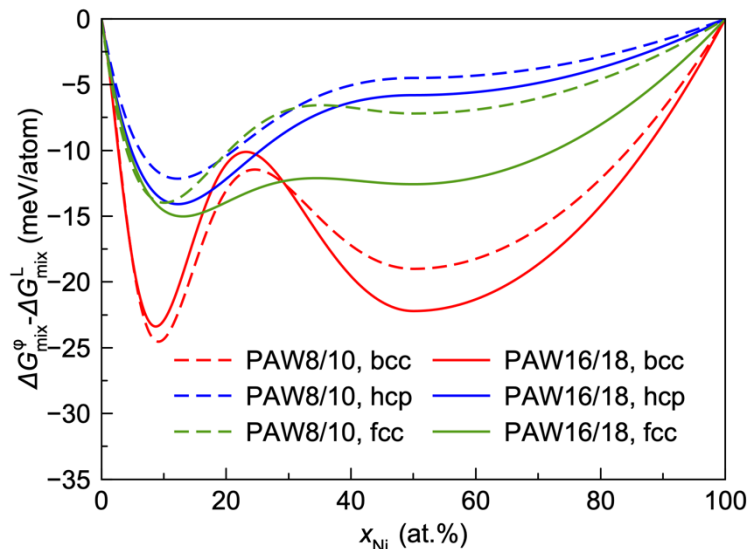


Figure S4. The relative Gibbs free energy of mixing. The relative Gibbs free energy of mixing using the liquid phase as the reference for phase φ , where φ is bcc, hcp, and fcc.

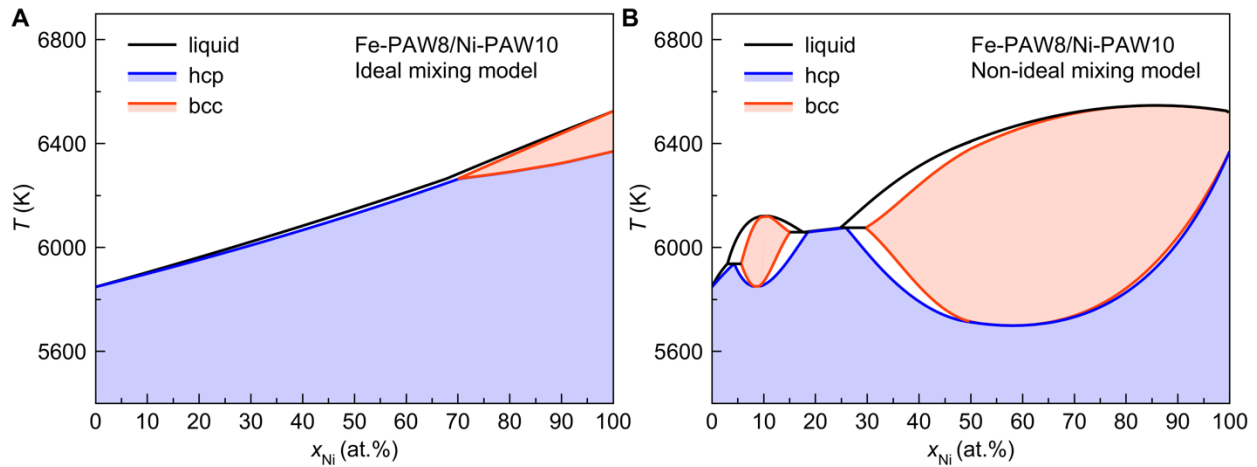


Figure S5. $\text{Fe}_{1-x}\text{Ni}_x$ phase diagrams at 323 GPa using different models without $3s^23p^6$ electron contributions. **A.** Ideal mixing model. **B.** Non-ideal mixing model.

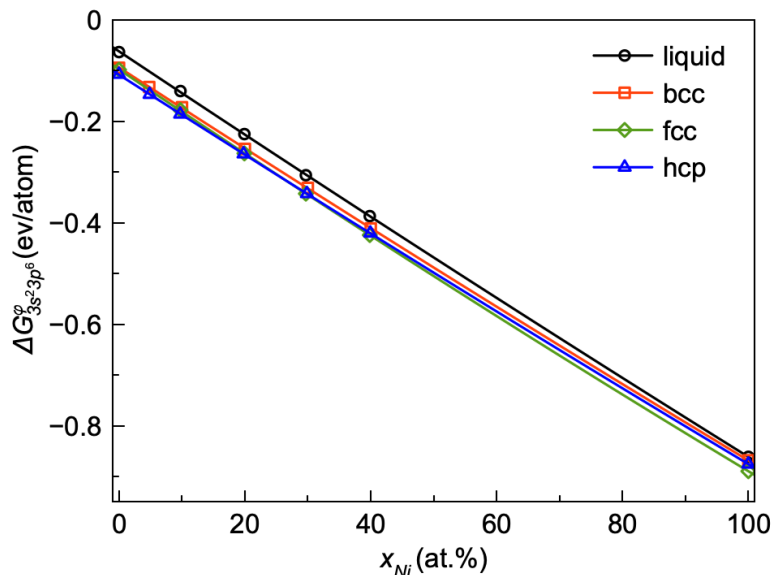


Figure S6. $3s^23p^6$ electron contributions. Free energy change caused by the inclusion of $3s^23p^6$ electrons in $\text{Fe}_{1-x}\text{Ni}_x$ phases at 323 GPa. $\Delta G_{3s^23p^6}^\varphi$ is defined in Eqn. (S10).

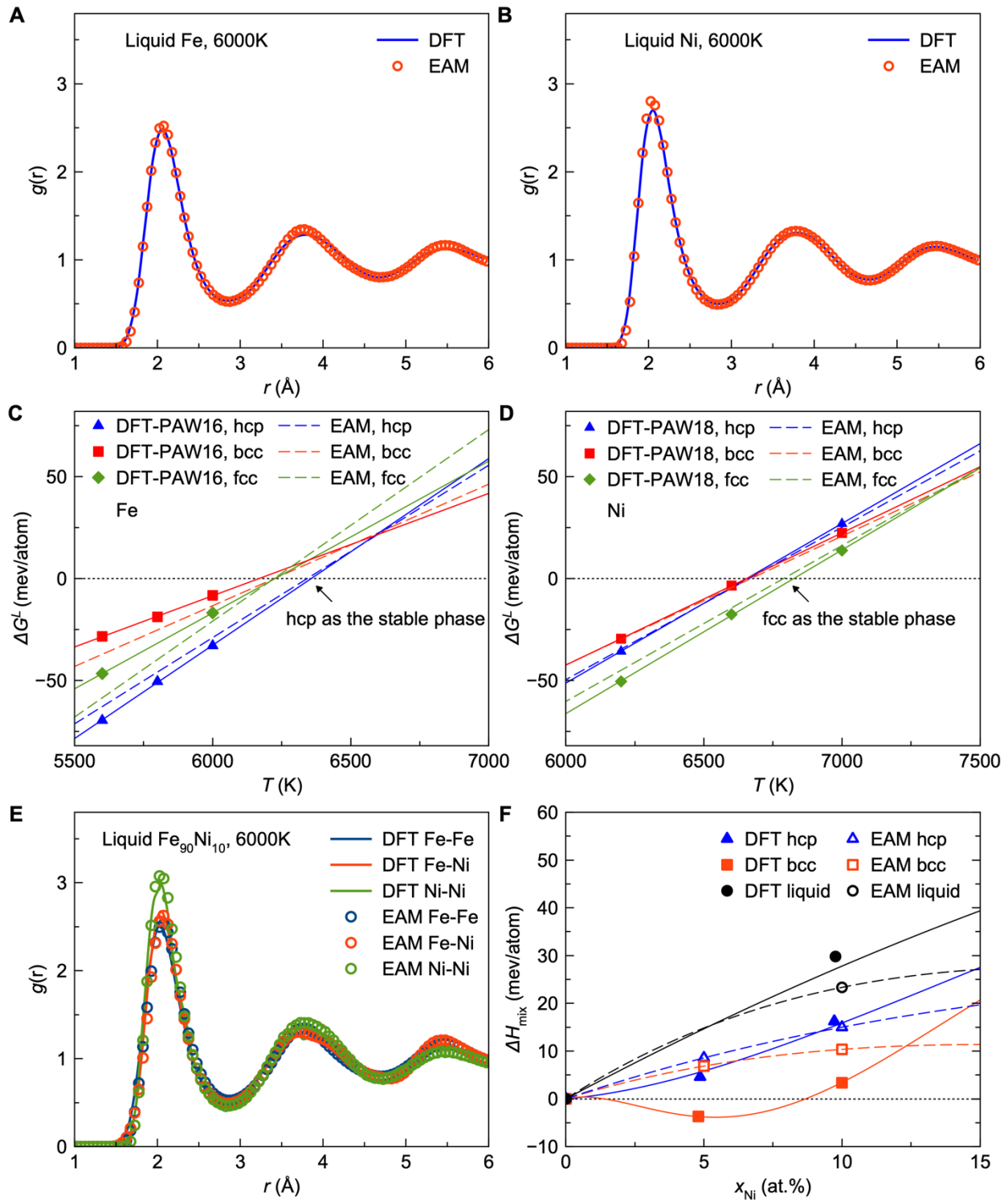


Figure S7. Thermodynamic properties of the EAM potential at 323 GPa. Pair correlation functions for **A.** Fe liquid, **B.** Ni liquid, and **E.** $\text{Fe}_{90}\text{Ni}_{10}$ at 6000 K. Gibbs free energy with respect to liquid phase ΔG^L of **C.** Fe and **D.** Ni. The arrows indicate that both the EAM and DFT results identify the most stable phases as hcp for Fe and fcc for Ni, respectively. **F.** Enthalpy of mixing for $\text{Fe}_{90}\text{Ni}_{10}$ phases. The dashed and solid lines are the fitting results for EAM and DFT, respectively.

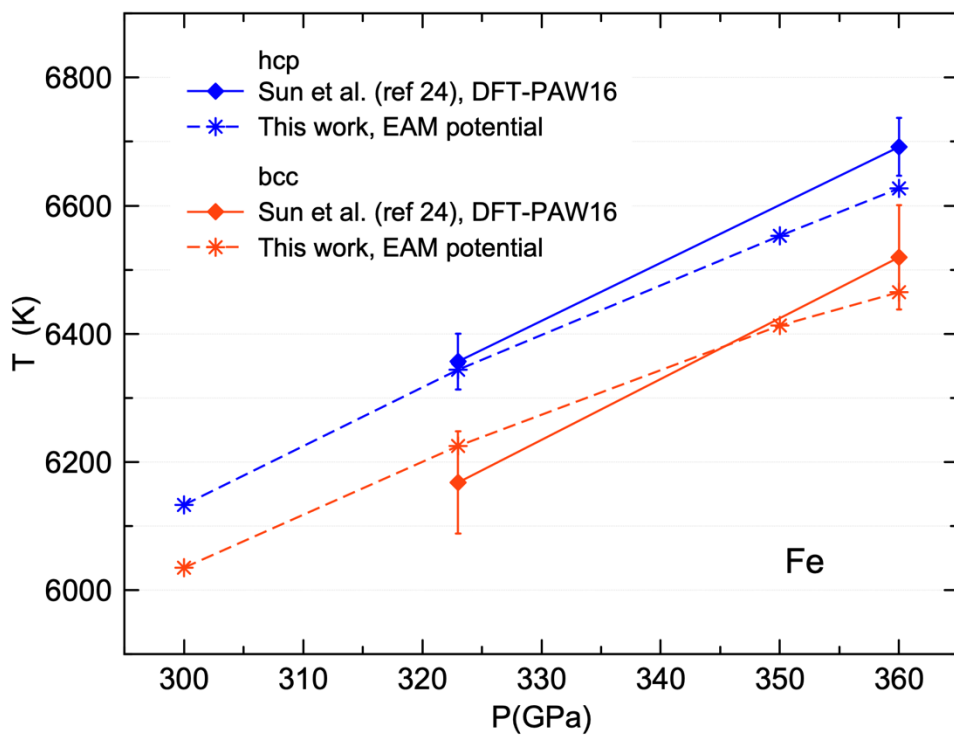


Figure S8. Melting curves of pure Fe. The melting temperatures are compared with the data from the previous *ab initio* calculations with PAW16 potential in Sun et al. (24).

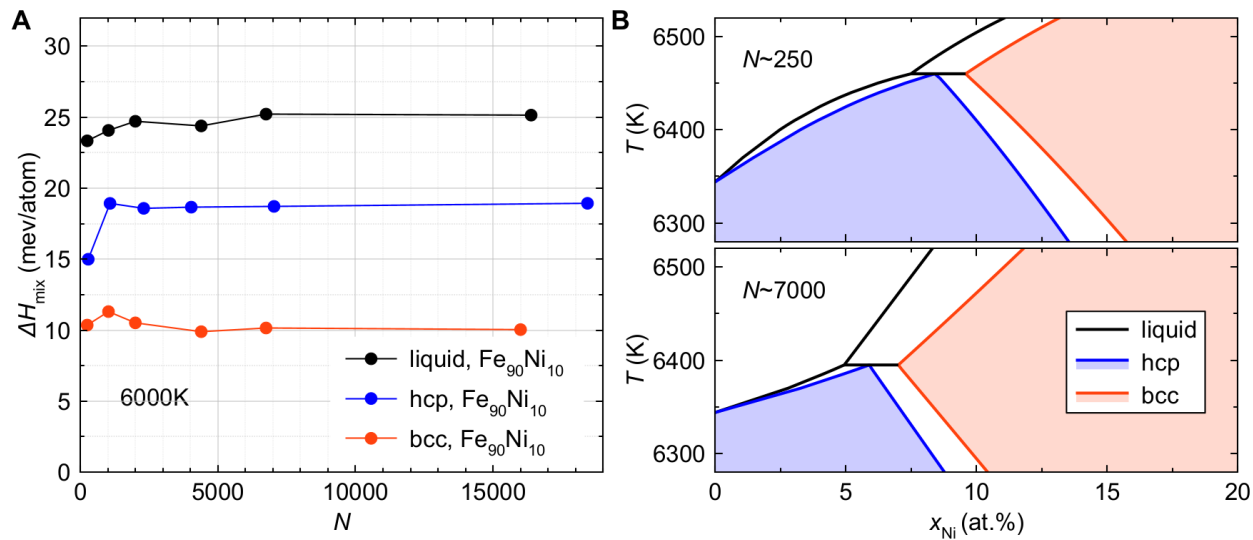


Figure S9. Size effect on the enthalpy of mixing and phase diagram. **A.** The enthalpy of mixing from MCMD simulations with different numbers of atoms for bcc, hcp, and liquid $\text{Fe}_{90}\text{Ni}_{10}$ at 323 GPa and 6000 K. **B.** FeNi phase diagram calculated by the solution model using the mixing enthalpy from small (~ 250 atoms) and large (~ 7000 atoms) simulation sizes.

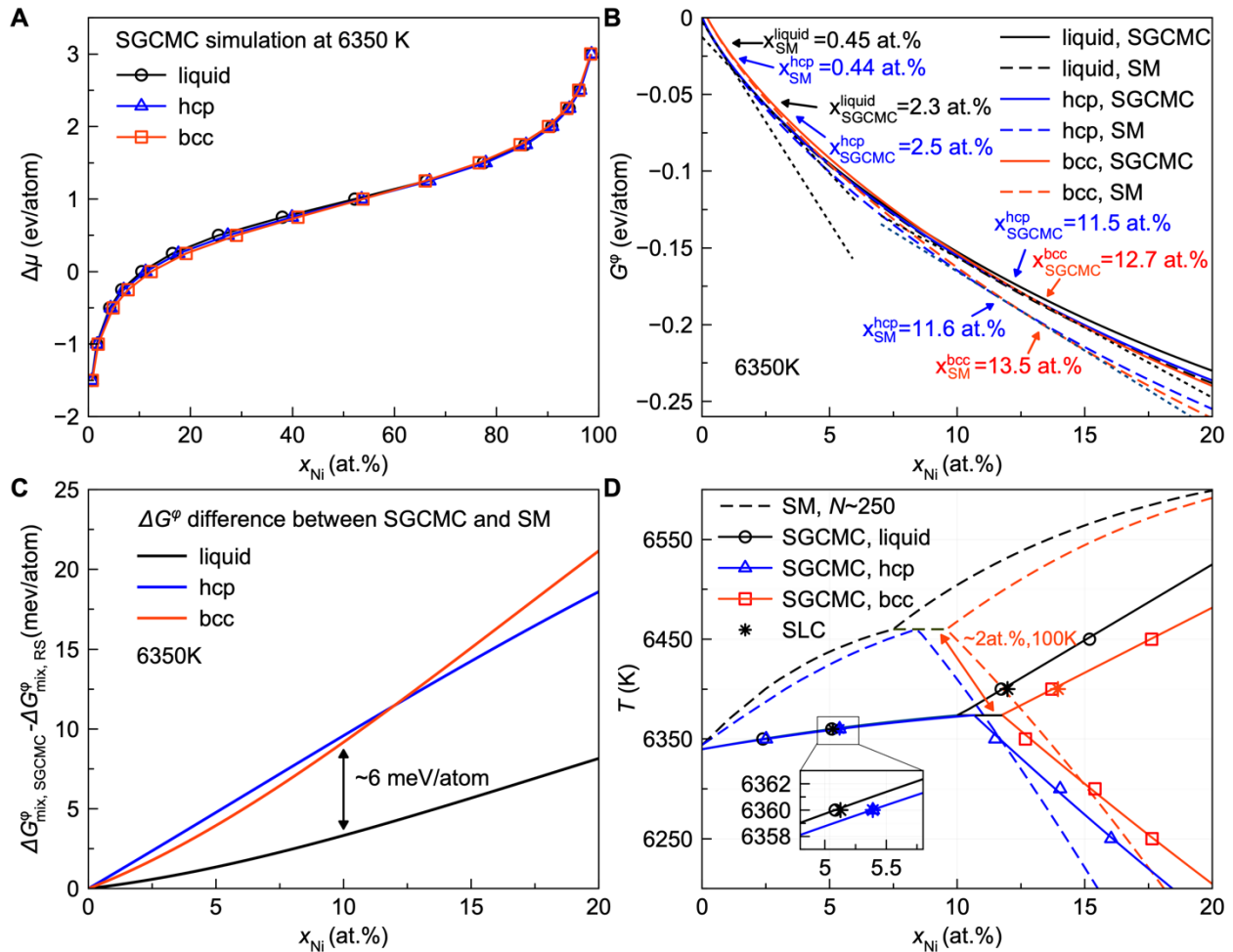


Figure S10. Gibbs free energy of the Fe-Ni solutions with EAM potential. **A.** The chemical potential as a function of Ni's composition from SGCMC simulations at 323 GPa and 6350 K. **B.** Comparison of Gibbs free energy between SGCMC and solution model (SM) for liquid, hcp, and bcc phases at 323 GPa and 6350 K. The dotted lines are the common tangent lines of Gibbs free energy for the two phases, which defines the coexisting composition. **C.** The difference in mixing free energy between the SGCMC and SM at 6350 K and 323 GPa. The arrow indicates the difference between liquid and hcp/bcc phases is $\sim 6 \text{ meV/atom}$ at 10 at.%. **D.** Phase diagram calculated by SM with ~ 250 atoms and SGCMC simulations at 323 GPa. The black, blue, and red lines represent the phase boundaries for the liquid, hcp, and bcc phases, respectively. The star symbols represent the equilibrated compositions from the SLC simulations. The arrow indicates the difference between the coexistence line is $\sim 2 \text{ at.\%}$ and 100 K.

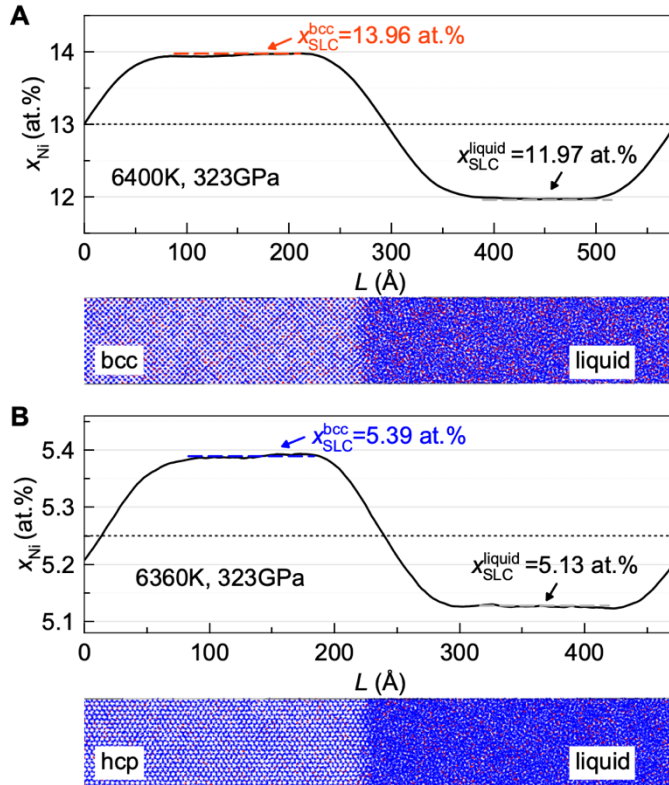


Figure S11. Solid-liquid coexistence simulations of $\text{Fe}_{1-x}\text{Ni}_x$ solutions. Ni concentration along the direction perpendicular to the solid-liquid interface for **A.** bcc-liquid coexistence and **B.** hcp-liquid coexistence. The dotted lines are the initial Ni concentration. The lower panel shows the equilibrated configurations. The blue and red dots represent Fe and Ni atoms, respectively.

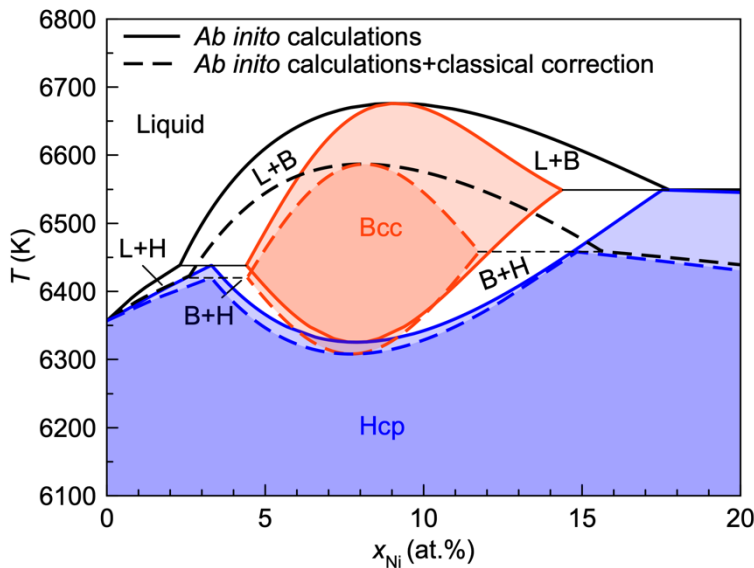


Figure S12. The uncertainty of the FeNi phase diagram from the *ab initio* calculations. The solid lines represent the phase diagram obtained using the solution model with pure *ab initio* calculations. The dashed lines represent the phase diagram with corrections for simulation size and non-ideal mixing entropy obtained via classical simulations with FeNi EAM potential.

Table S1. Enthalpy from MC+AIMD simulations. Enthalpy values from four independent simulations for the bcc, hcp, and fcc phases. The values in brackets in the last column represent the standard deviations.

Phase	Case	H (eV/atom) at 323 GPa	H _{ave} (eV/atom) at 323 GPa
bcc, Fe ₂₂₅ Ni ₂₅	1	8.7093	8.7106 (0.0016)
	2	8.7132	
	3	8.7094	
	4	8.7104	
hcp, Fe ₂₆₀ Ni ₂₈	1	8.5167	8.5169 (0.0001)
	2	8.5169	
	3	8.5171	
	4	8.5170	
fcc, Fe ₂₃₁ Ni ₂₅	1	8.5439	8.5434 (0.0005)
	2	8.5435	
	3	8.5438	
	4	8.5426	

REFERENCES AND NOTES

1. F. Birch, Elasticity and constitution of the Earth's interior. *J. Geophys. Res.* **57**, 227–286 (1952).
2. K. Hirose, S. Labrosse, J. Hernlund, Composition and state of the core. *Annu. Rev. Earth Planet. Sci.* **41**, 657–691 (2013).
3. O. L. Anderson, Properties of iron at the Earth's core conditions. *Geophys. J. Int.* **84**, 561–579 (1986).
4. G. Steinle-Neumann, L. Stixrude, R. E. Cohen, O. Gülsen, Elasticity of iron at the temperature of the Earth's inner core. *Nature* **413**, 57–60 (2001).
5. Y. Zhang, Y. Wang, Y. Huang, J. Wang, Z. Liang, L. Hao, Z. Gao, J. Li, Q. Wu, H. Zhang, Y. Liu, J. Sun, J.-F. Lin, Collective motion in hcp-Fe at Earth's inner core conditions. *Proc. Natl. Acad. Sci. U.S.A.* **120**, e2309952120 (2023).
6. L. Vočadlo, I. G. Wood, M. J. Gillan, J. Brodholt, D. P. Dobson, G. D. Price, D. Alfè, The stability of bcc-Fe at high pressures and temperatures with respect to tetragonal strain. *Phys. Earth Planet. Inter.* **170**, 52–59 (2008).
7. A. B. Belonoshko, T. Lukinov, J. Fu, J. Zhao, S. Davis, S. I. Simak, Stabilization of body-centred cubic iron under inner-core conditions. *Nat. Geosci.* **10**, 312–316 (2017).
8. K. Hirose, B. Wood, L. Vočadlo, Light elements in the Earth's core. *Nat. Rev. Earth Environ.* **2**, 645–658 (2021).
9. J. Liu, Y. Sun, C. Lv, F. Zhang, S. Fu, V. B. Prakapenka, C. Wang, K. Ho, J. Lin, R. M. Wentzcovitch, Iron-rich Fe–O compounds at Earth's core pressures. *Innovation* **4**, 100354 (2023).
10. Y. Tian, P. Zhang, W. Zhang, X. Feng, S. A. T. Redfern, H. Liu, Iron alloys of volatile elements in the deep Earth's interior. *Nat. Commun.* **15**, 3320 (2024).

11. T. Liu, Z. Jing, Hydrogen and silicon are the preferred light elements in Earth's core. *Commun. Earth Environ.* **5**, 1–8 (2024).
12. F. Sakai, K. Hirose, G. Morard, Partitioning of silicon and sulfur between solid and liquid iron under core pressures: Constraints on Earth's core composition. *Earth Planet. Sci. Lett.* **624**, 118449 (2023).
13. L. Yuan, G. Steinle-Neumann, Hydrogen distribution between the Earth's inner and outer core. *Earth Planet. Sci. Lett.* **609**, 118084 (2023).
14. V. F. Buchwald, *Handbook of Iron Meteorites. Their History, Distribution, Composition and Structure* (Arizona State University, 1975).
15. J.-F. Lin, D. L. Heinz, A. J. Campbell, J. M. Devine, W. L. Mao, G. Shen, Iron-nickel alloy in the Earth's core. *Geophys. Res. Lett.* **29**, 1471 (2002).
16. T. Komabayashi, Phase relations of Earth's core-forming materials. *Crystals* **11**, 581 (2021).
17. T. Komabayashi, K. Hirose, Y. Ohishi, In situ X-ray diffraction measurements of the fcc–hcp phase transition boundary of an Fe–Ni alloy in an internally heated diamond anvil cell. *Phys. Chem. Miner.* **39**, 329–338 (2012).
18. M. Ekholm, A. S. Mikhaylushkin, S. I. Simak, B. Johansson, I. A. Abrikosov, Configurational thermodynamics of Fe–Ni alloys at Earth's core conditions. *Earth Planet. Sci. Lett.* **308**, 90–96 (2011).
19. L. Dubrovinsky, N. Dubrovinskaia, O. Narygina, I. Kantor, A. Kuznetsov, V. B. Prakapenka, L. Vitos, B. Johansson, A. S. Mikhaylushkin, S. I. Simak, I. A. Abrikosov, Body-centered cubic iron-nickel alloy in Earth's core. *Science* **316**, 1880–1883 (2007).
20. T. Sakai, E. Ohtani, N. Hirao, Y. Ohishi, Stability field of the hcp-structure for Fe, Fe-Ni, and Fe-Ni-Si alloys up to 3 Mbar. *Geophys. Res. Lett.* **38**, 2011GL047178 (2011).

21. D. Ikuta, E. Ohtani, N. Hirao, Two-phase mixture of iron–nickel–silicon alloys in the Earth’s inner core. *Commun. Earth Environ.* **2**, 225 (2021).
22. Y. Sun, M. I. Mendelev, F. Zhang, X. Liu, B. Da, C.-Z. Wang, R. M. Wentzcovitch, K.-M. Ho, Unveiling the effect of Ni on the formation and structure of Earth’s inner core. *Proc. Natl. Acad. Sci. U.S.A.* **121**, e2316477121 (2024).
23. B. Martorell, J. Brodholt, I. G. Wood, L. Vočadlo, The effect of nickel on the properties of iron at the conditions of Earth’s inner core: Ab initio calculations of seismic wave velocities of Fe–Ni alloys. *Earth Planet. Sci. Lett.* **365**, 143–151 (2013).
24. Y. Sun, M. I. Mendelev, F. Zhang, X. Liu, B. Da, C. Wang, R. M. Wentzcovitch, K. Ho, Ab initio melting temperatures of Bcc and Hcp iron under the Earth’s inner core condition. *Geophys. Res. Lett.* **50**, e2022GL102447 (2023).
25. T. Sun, J. P. Brodholt, Y. Li L. Vočadlo, Melting properties from ab initio free energy calculations: Iron at the Earth’s inner-core boundary. *Phys. Rev. B* **98**, 224301 (2018).
26. S. Chatterjee, S. Ghosh, T. Saha-Dasgupta, Ni doping: A viable route to make body-centered-cubic Fe stable at Earth’s inner core. *Minerals* **11**, 258 (2021).
27. M. Widom, W. P. Huhn, S. Maiti, W. Steurer, Hybrid Monte Carlo/molecular dynamics simulation of a refractory metal high entropy alloy. *Metall. Mater. Trans. A* **45**, 196–200 (2014).
28. F. Wu, S. Wu, C.-Z. Wang, K.-M. Ho, R. Wentzcovitch, Y. Sun, Melting temperature of iron under the Earth’s inner core condition from deep machine learning. *Geosci. Front.* **15**, 101925 (2024).
29. S. Tateno, K. Hirose, T. Komabayashi, H. Ozawa, Y. Ohishi, The structure of Fe-Ni alloy in Earth’s inner core. *Geophys. Res. Lett.* **39**, 2–5 (2012).
30. Y. Sun, F. Zhang, M. I. Mendelev, R. M. Wentzcovitch, K.-M. Ho Two-step nucleation of the Earth’s inner core. *Proc. Natl. Acad. Sci. U.S.A.* **119**, e2113059119 (2022).

31. J. Wang, P. Jiang, F. Yuan, X. Wu, Chemical medium-range order in a medium-entropy alloy. *Nat. Commun.* **13**, 1021 (2022).
32. Z. An, T. Yang, C. Shi, S. Mao, L. Wang, A. Li, W. Li, X. Xue, M. Sun, Y. Bai, Y. He, F. Ren, Z. Lu, M. Yan, Y. Ren, C.-T. Liu, Z. Zhang, X. Han, Negative enthalpy alloys and local chemical ordering: A concept and route leading to synergy of strength and ductility. *Natl. Sci. Rev.* **11**, nwae026 (2024).
33. A. van de Walle, G. Ceder, The effect of lattice vibrations on substitutional alloy thermodynamics. *Rev. Mod. Phys.* **74**, 11–45 (2002).
34. R. M. Wentzcovitch, J. F. Justo, Z. Wu, C. R. S. da Silva, D. A. Yuen, D. Kohlstedt, Anomalous compressibility of ferropericlase throughout the iron spin cross-over. *Proc. Natl. Acad. Sci. U.S.A.* **106**, 8447–8452 (2009).
35. F. Wu, Y. Sun, T. Wan, S. Wu, R. M. Wentzcovitch, Deep-learning-based prediction of the tetragonal → cubic transition in davemaoite. *Geophys. Res. Lett.* **51**, e2023GL108012 (2024).
36. E. R. D. Scott, J. T. Wasson, Classification and properties of iron meteorites. *Rev. Geophys.* **13**, 527–546 (1975).
37. K. Łuszczek, T. A. Przylibski, Selected metal resources on H chondrite parent bodies. *Planet. Space Sci.* **206**, 105309 (2021).
38. R. A. Fischer, “Melting of Fe alloys and the thermal structure of the core” in *Deep Earth: Physics and Chemistry of the Lower Mantle and Core* (Geophysical Monograph Series, Wiley, 2016), pp. 1–12.
39. M. Pozzo, C. Davies, D. Gubbins, D. Alfè, Thermal and electrical conductivity of solid iron and iron–silicon mixtures at Earth’s core conditions. *Earth Planet. Sci. Lett.* **393**, 159–164 (2014).

40. D. Alfè, G. D. Price, M. J. Gillan, Iron under Earth's core conditions: Liquid-state thermodynamics and high-pressure melting curve from ab initio calculations *Phys. Rev. B* **65**, 165118 (2002).
41. H. Tkalčić, Complex inner core of the Earth: The last frontier of global seismology. *Rev. Geophys.* **53**, 59–94 (2015).
42. D. Tian, L. Wen, Seismological evidence for a localized mushy zone at the Earth's inner core boundary. *Nat. Commun.* **8**, 165 (2017).
43. B. Zhang, S. Ni, W. Wu, Z. Shen, W. Wang, D. Sun, Z. Wu, Small-scale layered structures at the inner core boundary. *Nat. Commun.* **14**, 6362 (2023).
44. G. Pang, K. D. Koper, S.-M. Wu, W. Wang, M. Lasbleis, G. Euler, Enhanced inner core fine-scale heterogeneity towards Earth's centre. *Nature* **620**, 570–575 (2023).
45. A. Morelli, A. M. Dziewonski, J. H. Woodhouse, Anisotropy of the inner core inferred from *PKIKP* travel times. *Geophys. Res. Lett.* **13**, 1545–1548 (1986).
46. M. Ishii, A. M. Dziewoński, The innermost inner core of the earth: Evidence for a change in anisotropic behavior at the radius of about 300 km. *Proc. Natl. Acad. Sci. U.S.A.* **99**, 14026–14030 (2002).
47. J. Stephenson, H. Tkalčić, M. Sambridge, Evidence for the innermost inner core: Robust parameter search for radially varying anisotropy using the neighborhood algorithm. *J. Geophys. Res. Solid Earth* **126** e2020JB020545 (2021).
48. H. Yang, P. Dou, T. Xiao, Y. Li, J. M. R. Muir, F. Zhang, The geophysical properties of FeHx phases under inner core conditions. *Geophys. Res. Lett.* **50**, e2023GL104493 (2023).
49. L. Huguet, J. A. Van Orman, S. A. Hauck, M. A. Willard, Earth's inner core nucleation paradox. *Earth Planet. Sci. Lett.* **487**, 9–20 (2018).

50. A. J. Wilson, D. Alfè, A. M. Walker, C. J. Davies, Can homogeneous nucleation resolve the inner core nucleation paradox? *Earth Planet. Sci. Lett.* **614**, 118176 (2023).
51. G. Kresse, J. Furthmüller, Efficient iterative schemes for *ab initio* total-energy calculations using a plane-wave basis set. *Phys. Rev. B* **54**, 11169–11186 (1996).
52. P. E. Blöchl, Projector augmented-wave method. *Phys. Rev. B* **50**, 17953–17979 (1994).
53. J. P. Perdew, K. Burke, M. Ernzerhof, Generalized gradient approximation made simple. *Phys. Rev. Lett.* **77**, 3865–3868 (1996).
54. N. D. Mermin, Thermal properties of the inhomogeneous electron gas. *Phys. Rev.* **137**, A1441–A1443 (1965).
55. R. M. Wentzcovitch, J. L. Martins, P. B. Allen, Energy versus free-energy conservation in first-principles molecular dynamics. *Phys. Rev. B* **45**, 11372–11374 (1992).
56. R. W. Zwanzig, High-temperature equation of state by a perturbation method. I. Nonpolar gases *J. Chem. Phys.* **22**, 1420–1426 (1954)
57. S. Nosé, A unified formulation of the constant temperature molecular dynamics methods. *J. Chem. Phys.* **81**, 511–519 (1984).
58. Z. Zhang, G. Csányi, D. Alfè, Partitioning of sulfur between solid and liquid iron under Earth's core conditions: Constraints from atomistic simulations with machine learning potentials. *Geochim. Cosmochim. Acta* **291**, 5–18 (2020).
59. Y. Huang, M. Widom, M. C. Gao, Ab initio free energies of liquid metal alloys: Application to the phase diagrams of Li-Na and K-Na *Phys. Rev. Mater.* **6**, 013802 (2022).
60. D. R. Gaskell, D. E. Laughlin, *Introduction to the Thermodynamics of Materials* (CRC Press, 2017).

61. L. Kaufman, H. Bernstein, *Computer Calculation of Phase Diagrams* (Academic Press, 1970).
62. M. C. Troparevsky, J. R. Morris, P. R. C. Kent, A. R. Lupini, G. M. Stocks, Criteria for predicting the formation of single-phase high-entropy alloys. *Phys. Rev. X* **5**, 011041 (2015).
63. C. Brooks, S. Lany, Heterostructural alloy phase diagram for $(\text{Cd}_{1-x}\text{Zn}_x)_3\text{As}_2$. *Phys. Rev. Mater.* **8**, L061201 (2024).
64. P. J. Spencer, A brief history of CALPHAD. *CAL* **32**, 1–8 (2008).
65. O. Redlich, A. T. Kister, Algebraic representation of thermodynamic properties and the classification of solutions. *Ind. Eng. Chem.* **40**, 345–348 (1948).
66. R. Otis, Z.-K. Liu, pycalphad: CALPHAD-based computational thermodynamics in Python *J. Open Res. Softw.* **5**, 1 (2017).
67. M. W. Finnis, J. E. Sinclair, A simple empirical N-body potential for transition metals. *Philos. Mag. A* **50**, 45–55 (1984).
68. M. I. Mendelev, D. J. Srolovitz, Determination of alloy interatomic potentials from liquid-state diffraction data. *Phys. Rev. B* **66**, 014205 (2002).
69. A. P. Thompson, H. M. Aktulga, R. Berger, D. S. Bolintineanu, W. M. Brown, P. S. Crozier, P. J. in't Veld, A. Kohlmeyer, S. G. Moore, T. D. Nguyen, R. Shan, M. J. Stevens, J. Tranchida, C. Trott, S. J. Plimpton, LAMMPS—A flexible simulation tool for particle-based materials modeling at the atomic, meso, and continuum scales. *Comput. Phys. Commun.* **271**, 108171 (2022).
70. B. Sadigh, P. Erhart, A. Stukowski, A. Caro, E. Martinez, L. Zepeda-Ruiz, Scalable parallel Monte Carlo algorithm for atomistic simulations of precipitation in alloys. *Phys. Rev. B* **85**, 184203 (2012).

71. D. A. Kofke, E. D. Glandt, Monte Carlo simulation of multicomponent equilibria in a semigrand canonical ensemble. *Mol. Phys.* **64**, 1105–1131 (1988).